University of Groningen

Massive Dark Matter Halos and Evolution of Early-Type Galaxies to z textasciitilde 1

Treu, Tommaso; Koopmans, Léon V.E.

IMPORTANT NOTE: You are advised to consult the publisher's version (publisher's PDF) if you wish to cite from it. Please check the document version below.

Document Version
Publisher's PDF, also known as Version of record

[Link to publication in University of Groningen/UMCG research database](#)

MASSIVE DARK MATTER HALOS AND EVOLUTION OF EARLY-TYPE GALAXIES TO $z \approx 1$[1]

TOMMASO TREU[2,3,4] AND LÉON V. E. KOOPMANS[5,6,7]

ABSTRACT

The combination of gravitational lensing and stellar dynamics breaks the mass-anisotropy degeneracy and provides stringent constraints on the distribution of luminous and dark matter in early-type (E/S0) galaxies out to $z \approx 1$. We present new observations and models of three lens systems (CFRS 03.1077, HST 14176+5226, HST 15433+5352) and the combined results from the five field E/S0 lens galaxies at $z \approx 0.5-1.0$ analyzed as part of the Lenses Structure and Dynamics (LSD) Survey. Our main results are as follows: (1) Constant mass-to-light ratio models are ruled out at greater than 99% CL for all five E/S0 galaxies, consistent with the presence of massive and extended dark matter halos. The range of projected dark matter mass fractions inside the Einstein radius is $f_{DM} = 0.37-0.72$, or 0.15–0.65 inside the effective radius R_e for isotropic models. (2) The average effective power-law slope of the total (luminous plus dark; $\rho_{tot} \propto r^{-\gamma'}$) mass distribution is $\langle\gamma'\rangle = 1.75 \pm 0.10$ (1.57 ± 0.16) for Osipkov-Merritt models with anisotropy radius $r_i = \infty$ (R_e) with an rms scatter of 0.2 (0.35), i.e., marginally flatter than isothermal ($\gamma' = 2$). The ratio between the observed central stellar velocity dispersion and that from the best-fit singular isothermal ellipsoid (SIE) lens model is $\langle f_{SIE}\rangle = \langle\sigma/\sigma_{SIE}\rangle = 0.87 \pm 0.04$ with 0.08 rms, consistent with flatter-than-isothermal density profiles. Considering that $\gamma' > 2$ and $f_{SIE} > 1$ have been reported for other systems (i.e., B1608+656 and PG 1115+080), we conclude that there is a significant intrinsic scatter in the slope of the mass-density profile of lens galaxies (rms $\sim$15%), similar to what is found for local E/S0 galaxies. Hence, the isothermal approximation is not sufficiently accurate for applications that depend critically on the slope of the mass-density profile, such as the measurement of the Hubble constant from time delays. (3) The average inner power-law slope γ of the dark matter halo is constrained to be $\langle\gamma\rangle = 1.3^{+0.2}_{-0.4}$ (68% CL), if the stellar velocity ellipsoid is isotropic ($r_i = \infty$), or an upper limit of $\gamma < 0.6$, if the galaxies are radially anisotropic ($r_i = R_e$). The observed range of slopes of the inner dark matter distribution is consistent with the results from numerical simulations only for an isotropic velocity ellipsoid and if baryonic collapse and star formation do not steepen dark matter density profiles. (4) The average stellar mass-to-light ratio evolves as $d\log(M_*/L_B)/dz = -0.72 \pm 0.10$, obtained via a fundamental plane analysis. An independent analysis based on lensing and dynamics gives an average $\langle d\log(M_*/L_B)/dz\rangle = -0.75 \pm 0.17$. Both values indicate that the mass-to-light ratio evolution for our sample of field E/S0 galaxies is slightly faster than those in clusters, consistent with the hypothesis that field E/S0 galaxies experience secondary bursts ($\sim$10% in mass) of star formation at $z < 1$. These findings are consistent with pure luminosity evolution of E/S0 galaxies in the past 8 Gyr and would be hard to reconcile with scenarios involving significant structural and dynamical evolution.

Subject headings: dark matter — galaxies: elliptical and lenticular, cD — galaxies: evolution — galaxies: formation — galaxies: structure — gravitational lensing

Online material: color figures

1. INTRODUCTION

A central assumption of the current standard ΛCDM cosmological model is that galaxies form and evolve inside dark matter halos (White & Rees 1978; Blumenthal et al. 1984; Davis et al. 1985). Dark matter halos are ubiquitous and possibly universal in their density profile (Navarro et al. 1996,

1997, hereafter collectively NFW; Moore et al. 1998), and they dominate the dynamics of large-scale structures. In spite of decades of searches and technological advances, our empirical knowledge of dark halos remains very sparse.

In the local universe, dark matter halos have been convincingly detected—predominantly through dynamical tracers—in spiral galaxies (e.g., Rubin et al. 1978, 1980; Faber & Gallagher 1979; van Albada & Sancisi 1986; Salucci & Burkert 2000; Jimenez et al. 2003), dwarf and low surface brightness galaxies (de Blok & McGaugh 1997; van den Bosch et al. 2000; Swaters et al. 2000), clusters of galaxies (Zwicky 1937; Kneib et al. 1993; Lombardi et al. 2000; Sand et al. 2002, 2004; Kneib et al. 2003), and, at least in some cases, early-type galaxies (e.g., Fabbiano 1989; Mould et al. 1990; Matsushita et al. 1998; Loewenstein & White 1999; Saglia et al. 1992; Bertin et al. 1994; Arnaboldi et al. 1996; Franx et al. 1994; Carollo et al. 1995; Rix et al. 1997; Gerhard et al. 2001; Borriello et al. 2003; Seljak 2002). However, observational evidence regarding dark matter halos of early-type galaxies (E/S0s) is limited. In a number of cases, constant

---

[2] Department of Physics and Astronomy, UCLA, Box 951547, Knudsen Hall, Los Angeles, CA 90095; ttreu@astro.ucla.edu.
[3] Hubble Fellow.
[4] Astronomy Option, California Institute of Technology, MS 105-24, Pasadena, CA 91125.
[5] Space Telescope Science Institute, 3700 San Martin Drive, Baltimore, MD 21218.
[6] Theoretical Astrophysics, California Institute of Technology, MS 130-33, Pasadena, CA 91125.
[7] Current address: Kapteyn Astronomical Institute, P.O. Box 800, 9700 AV Groningen, Netherlands.

mass-to-light models, with a mass-to-light ratio consistent with those of a normal stellar population, appear sufficient to explain the information available from mass tracers, and there is no need to invoke the existence of dark matter halos (e.g., Bertin et al. 1994; Romanowsky et al. 2003).

If detection of dark matter is hard and often ambiguous, decomposing the mass distribution into a luminous (mostly stellar) and dark matter component, to measure their relative contribution and spatially resolved properties, has been possible in only very few cases with varying results (see references above). The main hurdles to overcome are the paucity of dynamical tracers at large radii (such as H I gas in spirals) and the degeneracy between kinematic properties of dynamical tracers (e.g., anisotropy for stellar dynamics) and the mass distribution. For simplicity, we refer to the latter problem as the mass-anisotropy degeneracy.

The distant universe ($z > 0.1$) is an almost completely uncharted territory. Gravitational lensing has provided evidence for a mass distribution that is more extended than the stellar component, either by the analysis of individual systems or by considering statistical ensembles (e.g., Kochanek 1995; Rusin & Ma 2001; Ma 2003; Rusin et al. 2002, 2003a; Cohn et al. 2001; Muñoz et al. 2001; Winn et al. 2003; Wucknitz et al. 2004). Unfortunately, for most lenses it has proven very difficult to reliably separate the luminous from the dark matter component using lensing alone and determine a precise dark matter density profile and mass fraction.

In spite of the difficulties, a detailed exploration of high-z galaxies would come with a great reward, offering the opportunity to map directly the evolution of dark and stellar mass over cosmic time. By mapping the time (i.e., redshift) evolution of the relative distributions of luminous and dark matter in early-type galaxies, as well as the evolution of stellar mass-to-light ratio and the slope of dark matter halos, we can address directly the following questions: How and when is mass assembled to form early-type galaxies? What is their star formation history? Are dark matter halos characterized by cuspy mass profiles in the center as predicted by numerical simulations? What is the role of star formation in shaping the total mass distribution of early-type galaxies? Do isolated early-type galaxies undergo internal structural/dynamical evolution?

To answer these questions, we are undertaking the Lenses Structure and Dynamics (LSD) Survey (Koopmans & Treu 2002, 2003; Treu & Koopmans 2002a, 2003; hereafter KT02, KT03, TK02a, TK03, or collectively KT). The survey takes advantage of the fact that distant early-type galaxies are efficient gravitational lenses. By focusing on lens galaxies, we can use gravitational lensing analyses to provide a precise and accurate mass measurement (typically 1–5 effective radii R_e), replacing very effectively the traditional dynamical tracers at large radii (e.g., X-ray; planetary nebulae or globular clusters kinematics) that cannot be used in the distant universe. The lensing analysis is then combined with stellar kinematic measurements, which provide constraints on the mass distribution at smaller radii (typically $\lesssim R_e$). The combination of the two diagnostics has proved to be very effective (KT) since they complement each other: lensing provides a robust integrated mass measurement, breaking the mass-anisotropy degeneracy of the stellar dynamical analysis, after which stellar dynamics provides a handle on the mass density profile of the lens.

The target lenses were selected from the sample of known galaxy-scale systems (see, e.g., the CASTLES Web site[8]) for

their morphology (E/S0), brightness of the lens ($I \lesssim 22$) and favorable contrast between the lens and the source to allow for internal kinematic measurements, and relative isolation (e.g., no rich clusters nearby) to simplify as much as possible the lens model and reduce the related uncertainties.

Spectroscopic observations using the Keck telescopes have now been completed (a total of nine allocated nights between 2001 July and 2002 December), yielding exquisite internal kinematics for many systems, including nine early-type E/S0 lens galaxies in the range $z \sim 0.1–1.0$. In this paper we present new data and models for three lenses: CFRS 03.1077 (Crampton et al. 2002; Hammer et al. 1995; Lilly et al. 1995; $z_l = 0.938$, $z_s = 2.941$ for the lens and source, respectively), HST 1417+5226 (Ratnatunga et al. 1995; Crampton et al. 1996; $z_l = 0.810$, $z_s = 3.399$), and HST 1543+5352 (Ratnatunga et al. 1999a; the newly measured redshifts are $z_l = 0.497$, $z_s = 2.092$). We refer to these lenses as C0302, H1417, and H1543, respectively. Note that all three objects were serendipitously discovered from *Hubble Space Telescope* (*HST*) images, i.e., the Groth Strip Survey (Groth et al. 1994), the Medium Deep Survey (Ratnatunga et al. 1999b), and the *HST* follow-up to the Canada-France Redshift Survey (Brinchmann et al. 1998). Together with the analyses of the systems MG 2016 and 0047 already presented by KT02, TK02a, and KT03, this completes the sample of the five high-redshift ($z \sim 0.5–1.0$) pressure-supported systems targeted by the LSD Survey so far. An analysis of the sample properties is presented here. The data and analysis of the lower redshift systems and partly rotationally supported systems in the current sample will be presented in forthcoming papers.

The paper is organized as follows. In § 2 we present *HST* imaging and Keck spectroscopic observations of the three lens systems. In § 3 we use the photometric and kinematic measurements to compare the sample of E/S0 lens galaxies to the local fundamental plane (FP; Djorgovski & Davis 1987; Dressler et al. 1987). The offset from the local FP is used to measure the redshift evolution of the stellar mass-to-light ratio and thereby constrain their star formation history. In § 4 we present gravitational lens models of the three lenses, using a modeling technique based on a nonparametric source reconstruction (e.g., Wallington et al. 1996, hereafter W96; Warren & Dye 2003, hereafter WD03) to fully take advantage of the extended nature of the multiply imaged sources. In § 5 we introduce two-component (luminous plus dark matter) mass models that are used in § 6 to perform a joint lensing and dynamics analysis and derive limits on the stellar mass-to-light ratio, on the inner slope of the dark matter halo, and on the total mass density profile of the sample of E/S0 galaxies. We also consider the complete sample of five high-redshift lenses and discuss the evolution of the stellar mass-to-light ratio in terms of stellar population and structural/dynamical evolution, the dark matter mass fraction, and the limits on the inner slope of the dark matter halos from a joint statistical analysis of the sample. In § 7 we discuss the homogeneity of the mass distribution of the lens galaxy population and its implication for lens-based studies such as the determination of the Hubble constant from gravitational time delays, evolution of early-type galaxies, and the determination of cosmological parameters from lens statistics. A final summary is given in § 8, and conclusions are drawn in § 9.

In the following, we assume that the Hubble constant, the matter density, and the cosmological constant are $H_0 = 65 \ h_{65}$ km s^{-1} Mpc^{-1} with $h_{65} = 1$, $\Omega_m = 0.3$, and $\Omega_\Lambda = 0.7$, respectively. Throughout this paper, r is the radial coordinate

---

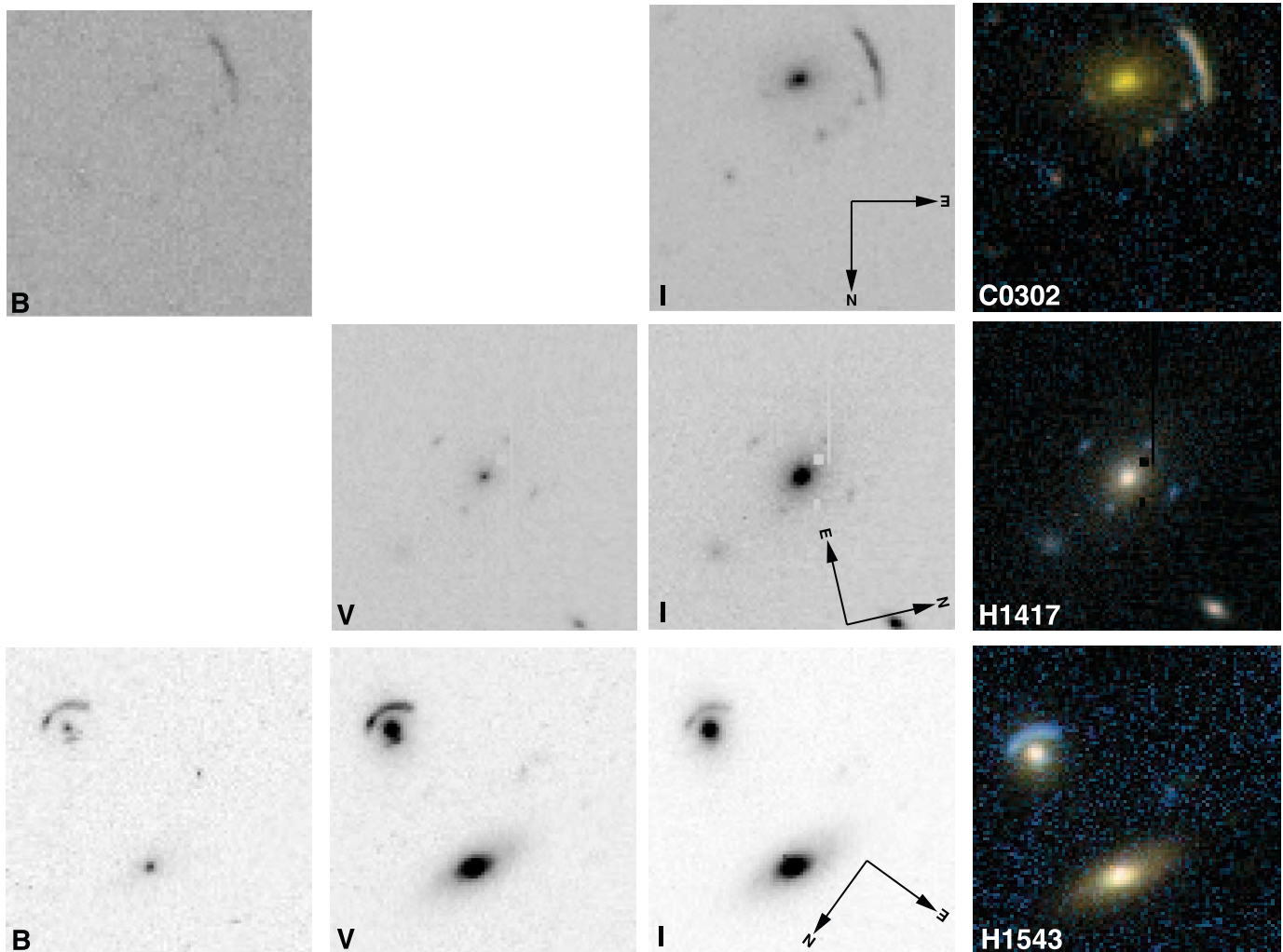[8] Available at http://cfa-www.harvard.edu/castles.

FIG. 1.—*HST* WFPC2 images in *B*, *V*, and *I* band of the three gravitational lens systems. The right panels show a color composite image. The image sizes are $8'' \times 8''$ for C0302 and $10'' \times 10''$ for H1417 and H1543, and the compass indicates the orientation of the images on the sky. Note the bright galaxy G2 ($z = 0.506$) next to the lens in H1543. C0302 is shown off-center because it is close to the edge of the WFPC2 chip.

in three-dimensional space, while *R* is the radial coordinate in two-dimensional projected space.

2. OBSERVATIONS

2.1. *HST Imaging*

Wide Field Planetary Camera 2 (WFPC2) images of the systems CFRS 03.1077, HST 1417+5226, and HST 1543+5352 are available from the *HST* archive. Five exposures each through the F450W filter and the F814W filter are available for C0302, with a total exposure time of 7000 and 6700 s, respectively. Four exposures (4400 s) are available for H1417 through F814W. Sixteen exposures are available through filter F606W at three different position angles, with a total exposure time of 11,200 s. For HST 1543, three exposures are available through filter F450W (8800 s), three through F606W (9000 s), and two through F814W (6000 s).

The images were reduced using a series of IRAF scripts based on the IRAF package DRIZZLE (Fruchter & Hook 2002), to align the different pointings and perform cosmic-ray rejection. The images were combined on a $0''.1$ pixel scale. An exception was made for the images of H1417 through F606W, which were combined in three groups according to the *HST*

P.A., to avoid problems related to distortion correction and complications of the azimuthal structure of the point-spread function (PSF). The reduced images of the galaxies are shown in Figure 1 together with color composite images. Note that for H1417 only the F606W images at the same P.A. as for the F814W ones are shown and that in these images a bad column of WFPC2 runs very close to one of the multiple images, although this is not the case for the other two sets of F606W images (not shown).

Surface photometry was performed on the F606W and F814W images as described in Treu et al. (1999, 2001b, hereafter T99, T01b). The F450W images were not used for surface photometry given the low signal-to-noise ratio of the (red) lens galaxies and the large contamination from the (blue) multiple images. The galaxy brightness profiles are well represented by an $R^{1/4}$ profile, which we fit, taking the *HST* PSF into account, to obtain the effective radius (R_e), the effective surface brightness (SB$_e$), and the total magnitude. The relevant observational quantities of the lens galaxies and their errors are listed in Table 1. The errors on SB$_e$ and R_e are tightly correlated, and the uncertainty on the combination $\log R_e - 0.32$SB$_e$ that enters the FP (see § 3) is very small ($\sim$0.015; see Kelson et al. 2000; T01b; Bertin et al. 2002). The rest-frame

TABLE 1
Observed Spectrophotometric Quantities

Lens	C0302	H1417	H1543
Redshift (lens).........................	0.938 ± 0.001	0.810 ± 0.001	0.497 ± 0.001
Redshift (source)....................	2.941 ± 0.001	3.399 ± 0.001	2.092 ± 0.001
F814W (mag).........................	19.86 ± 0.11	19.59 ± 0.05	20.22 ± 0.10
F606W (mag).........................	...	21.53 ± 0.05	20.66 ± 0.11
$SB_{e,F814W}$ (mag arcsec^{-2}).......	22.87 ± 0.13	21.71 ± 0.12	20.30 ± 0.10
$SB_{e,F606W}$ (mag arcsec^{-2}).......	...	24.06 ± 0.14	21.80 ± 0.11
$R_{e,F814W}$ (arcsec)	1.60 ± 0.15	1.06 ± 0.08	0.41 ± 0.04
$R_{e,F606W}$ (arcsec)	...	1.29 ± 0.13	0.42 ± 0.04
$b/a = (1-e)$.........................	0.75 ± 0.05	0.85 ± 0.05	0.95 ± 0.05
Major-axis P.A. (deg).............	-72 ± 5	34 ± 5	56 ± 5
σ (km s^{-1})...............................	251 ± 19	224 ± 15	116 ± 10
$M_V - 5 \log h_{65}$ (mag)..............	...	...	-21.40 ± 0.10
$M_B - 5 \log h_{65}$ (mag)..............	-23.30 ± 0.1	-22.98 ± 0.055	-20.63 ± 0.11
$R_{e,V}$ (h_{65}^{-1} kpc)	...	...	2.7 ± 0.3
$R_{e,B}$ (h_{65}^{-1} kpc)	14.1 ± 1.3	8.6 ± 0.6	2.8 ± 0.3
$SB_{e,V}$ (mag arcsec^{-2})..............	...	...	19.34 ± 0.10
$SB_{e,B}$ (mag arcsec^{-2})..............	20.92 ± 0.14	20.25 ± 0.12	20.16 ± 0.11

Notes.—The second part of the table (starting with σ) lists rest-frame quantities, derived from the observed quantities as described in § 2. Note that σ is the central velocity dispersion corrected to a circular aperture of radius $R_e/8$. All quantities in this table assume $H_0 = 65$ km s^{-1} Mpc^{-1}, $\Omega_m = 0.3$, and $\Omega_\Lambda = 0.7$.

photometric quantities listed in Table 1, computed as described in T01b, are corrected for Galactic extinction using $E(B-V)$ from Schlegel et al. (1998).

Astrometry for the system H1417—the only one for which the lensed images can be approximated as point images—was derived from the two sets of six exposures through filter F606W that are not affected by a bad column. The two astrometries agree within the uncertainties and are averaged to determine the relative offsets between the lens galaxy and the multiple images used to constrain the lens model in § 4.

2.2. Keck Spectroscopy

The lens galaxies were observed using the Echelle Spectrograph and Imager (ESI; Sheinis et al. 2002) at the Keck II telescope during four runs on 2001 July 21–26, 2002 February 7–8, 2002 June 6, and 2002 December 7–8. Conditions were generally photometric with episodes of thin cirrus. Between each exposure, we dithered along the slit to allow for a better removal of sky residuals in the red end of the spectrum. The slit (20″ in length) was aligned with the major axis of the lens galaxy (C0302, H1417) or slightly tilted as to include the massive nearby companion (H1543; Fig. 1). ESI was used in high-resolution mode with a 1″25 wide slit, yielding a resolution of ∼30 km s^{-1}, adequate for measuring the stellar velocity dispersion and removing narrow sky

emission lines. The centering of the lens galaxies in the slit was constantly monitored by means of the ESI viewing camera (all galaxies were bright enough to be visible in a few second exposure), and we estimate the centering perpendicular to the slit to be accurate to ≲0″1. Additional details of the observing runs are given in Table 2. The ESI data were reduced using the IRAF package EASI2D[9] as described in KT. The redshifts of the lenses are given in Table 1.

First, the full integrated spectra were used to derive the central velocity dispersion of the lens galaxies with maximal accuracy. The aperture velocity dispersions are measured by comparing broadened stellar templates with the observed galaxy spectra in pixel space, as described in T99, Treu et al. (2001a, hereafter T01a), KT02, and KT03. They are subsequently converted into a central velocity dispersion (i.e., within a circular aperture of radius $R_e/8$), applying an upward correction factor of 1.08 ± 0.04 (T01a). The central velocity dispersion of G2—the massive companion to H1543 at $z = 0.506$ (see Fig. 1)—is found to be $\sigma = 263 \pm 11$ km s^{-1}, by applying the same procedure.

Second, we derive spatially resolved kinematic profiles in the following manner. For each galaxy, we define three symmetric spectroscopic apertures centered on the lens galaxy,

---

[9] EASI2D was developed by D. Sand and T. Treu (Sand et al. 2002, 2004).

TABLE 2
Spectroscopic Observing Log

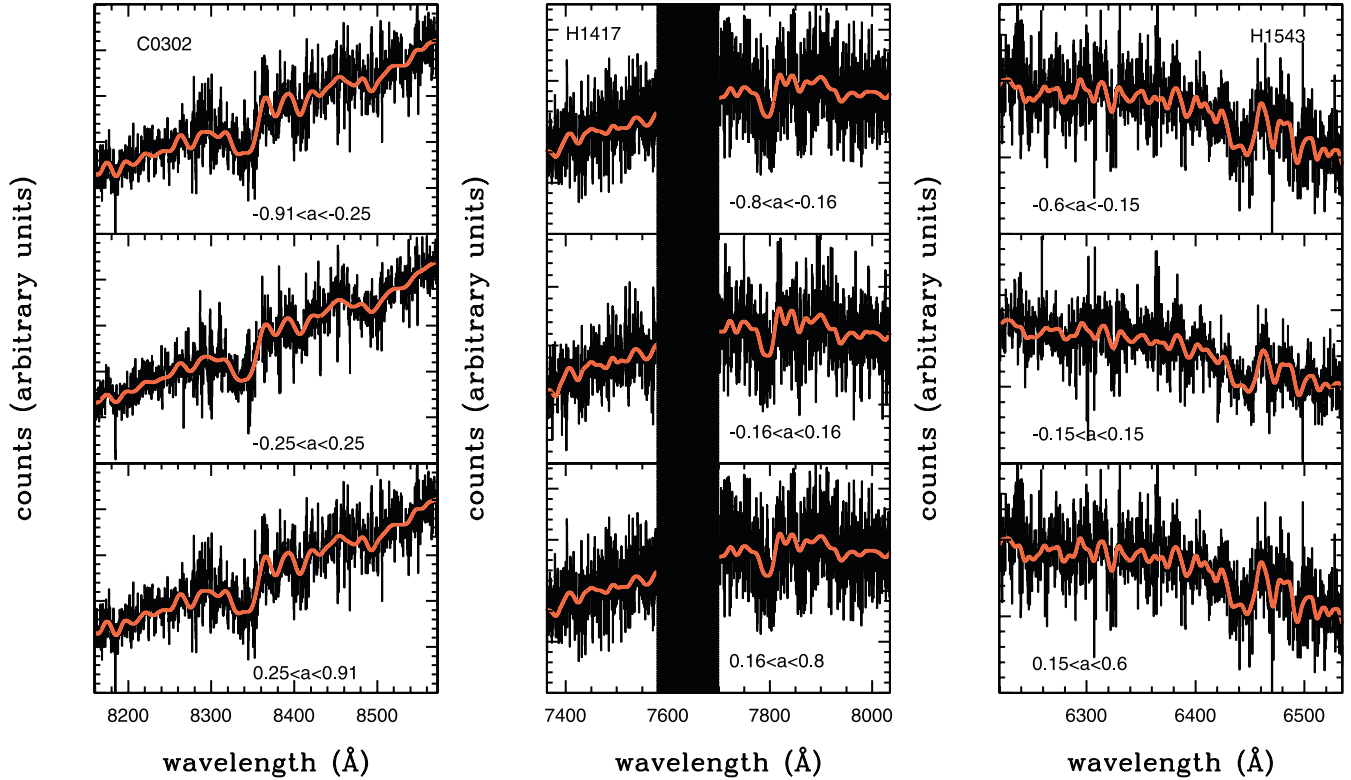| Galaxy	Instrument	Date	Seeing (arcsec)	Exposure Time (s)	P.A. (deg)
C0302....................	ESI	2002 Dec 7, 8	0.8	23400	110
H1417....................	ESI	2002 Feb 7	0.8	6300	37.2
H1417....................	ESI	2001 Jul 25, 26	0.7	7200	37.2
H1543....................	ESI	2002 Jun 6	0.6	14400	68
H1543....................	LRIS	2003 Mar 5	1.0	5400	142

Fig. 2.—Keck ESI spectra of the E/S0 lens galaxies in C0302, H1417, and H1543. A stellar template broadened to the best-fitting velocity dispersion is overplotted. The bin sizes along the major axes are indicated in arcseconds. The width of the bins is 1″25.

such that the signal-to-noise ratio of the spectra integrated within each aperture is sufficient to measure[10] a stellar velocity dispersion (see the discussion in Koopmans et al. 2003, hereafter K03). Portions of the spectra of the lens galaxies around the G band (4304 Å) for each spectroscopic aperture are shown in Figure 2. The apertures are listed in Table 3 together with the measured stellar velocity dispersions. Note that our measurement of the central velocity dispersion of H1417, $\sigma = 224 \pm 15$ km s^{-1}, is in excellent agreement

---

[10] Using the Gauss-Hermite pixel fitting software (van der Marel 1994), as described, e.g., in T01a.

TABLE 3
KINEMATIC DATA ALONG THE MAJOR AXIS OF THE LENSES

Galaxy	Aperture (arcsec^2)	σ (km s^{-1})	$\Delta\sigma$ (km s^{-1})	S/N (Å^{-1})
C0302............	$(-0.91:-0.25) \times 1.25$	195	17	12
	$(-0.25:+0.25) \times 1.25$	256	19	14
	$(+0.25:+0.91) \times 1.25$	234	23	11
H1417............	$(-0.80:-0.16) \times 1.25$	223	20	13
	$(-0.16:+0.16) \times 1.25$	212	18	15
	$(+0.16:+0.80) \times 1.25$	199	22	12
H1543............	$(-0.60:-0.15) \times 1.25$	77	14	12
	$(-0.15:+0.15) \times 1.25$	108	14	13
	$(+0.15:+0.60) \times 1.25$	124	19	12
H1543 (G2)........	$(-0.38:+0.38) \times 1.25$	253	10	25

NOTE.—The adjacent rectangular apertures are indicated, as well as the measured aperture velocity dispersions (σ), their uncertainty ($\Delta\sigma$), and the average S/N per Å in the region used for the kinematic fit.

with the two measurements that have been published so far: Ohyama et al. (2002) found $\sigma_{ap} = 230 \pm 14$ km s^{-1} within an aperture equivalent to a circular aperture of radius 0″4; Gebhardt et al. (2003) measure $\sigma_{ap} = 202 \pm 9$ km s^{-1} within their spectroscopic aperture, which they correct to a central velocity dispersion of $\sigma = 222 \pm 10$ km s^{-1}.

Since the ESI spectra did not yield the redshift for the lensed arc in H1543, additional spectra were obtained using the Low Resolution Imaging Spectrometer (LRIS; Oke et al. 1995) on 2003 March 5, to exploit the favorable contrast at the blue end of the spectrum. The 1″0 slit was centered on the arc and aligned with the parallactic angle (Table 2). The blue end of the spectrum (Fig. 3) reveals a set of UV absorption lines typical of Lyman break galaxies (Steidel et al. 1996) that unambiguously yields the redshift of the arc as $z_s = 2.092 \pm 0.001$.

3. THE FUNDAMENTAL PLANE AND THE EVOLUTION OF THE STELLAR POPULATIONS

Early-type galaxies in the local universe occupy approximately a plane in the three-dimensional space defined by the effective radius ($\log R_e$), effective surface brightness (SB$_e$), and central velocity dispersion ($\log \sigma$),

$$\log R_e = \alpha_{FP} \log \sigma + \beta_{FP} SB_e + \gamma_{FP}, \quad (1)$$

known as the fundamental plane (FP; Dressler et al. 1987; Djorgovski & Davis 1987).

Under appropriate assumptions (e.g., T01a), the evolution of the FP with redshift can be used to measure the star formation histories of early-type galaxies (e.g., Franx 1993). Specifically, if we can define an effective mass $M \propto \sigma^2 R_e$, and
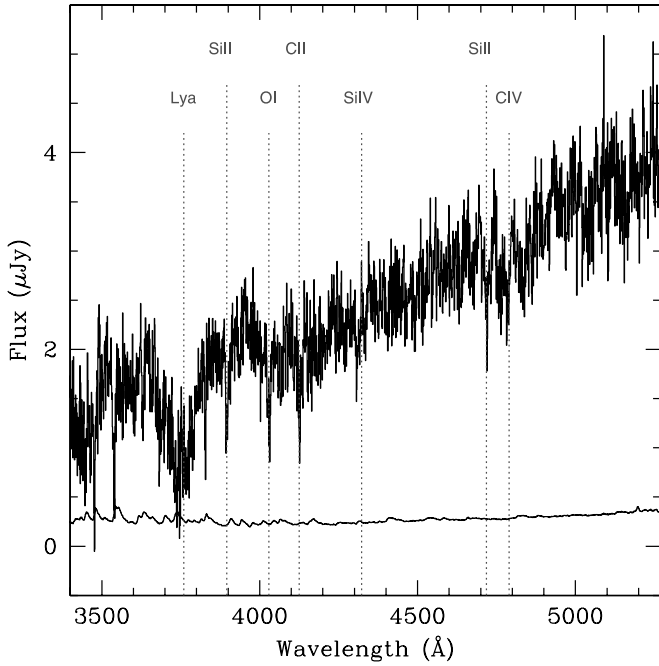
FIG. 3.—Keck LRIS spectrum (3400–5300 Å) of the lensed source in H1543. Multiple absorption features clearly identify a redshift of $z_s = 2.092$. The lower curve represents the noise level. [*See the electronic edition of the Journal for a color version of this figure.*]

FIG. 4.—Evolution of the FP in rest-frame *B* band. Filled squares with error bars are the E/S0 lens galaxies analyzed in this paper. The thick solid line (TK04) is a linear fit to these points. The other lines represent linear fits to measurements from the literature for the field FP (T02 = Treu et al. 2002; G03 = Gebhardt et al. 2003; vDE03 = van Dokkum & Ellis 2003; vdW04 = van der Wel et al. 2004), the cluster FP (vD98 = van Dokkum et al. 1998), and the FP based on estimates of $\sigma_{\rm SIE}$ using the method of Kochanek et al. 2000 (R03 = Rusin et al. 2003b; vdV03 = van de Ven et al. 2003). Note that the linear fits of T02, TK04 (this paper), and vdW04 are almost identical. See text for details.

if there is no evolution of the slopes $\alpha_{\rm FP}$ and $\beta_{\rm FP}$, the evolution of the intercept can be used to measure the evolution of the average effective mass-to-light ratio $\Delta \log (M/L) = -0.4\Delta\gamma_{\rm FP}/\beta_{\rm FP}$ (e.g., van Dokkum & Franx 1996; Kelson et al. 1997; Bender et al. 1998; Pahre 1998; van Dokkum et al. 1998; Jørgensen et al. 1999; T99; Treu et al. 2002, hereafter T02; Ziegler et al. 2001; van Dokkum & Stanford 2003; van Dokkum & Ellis 2003; Gebhardt et al. 2003; van der Wel et al. 2004). In the following analysis we adopt as a reference the local FP from Bender et al. (1998), i.e., $\alpha = 1.25$, $\beta = 0.32$, and $\gamma_{\rm FP} = -8.895 - \log h_{50}$, noting that our results do not depend critically on the adopted coefficients of the local FP (e.g., T99; T02).

3.1. *Stellar Mass-to-Light Evolution from the FP*

In Figure 4 we plot the evolution of the effective *M/L* for the five lens galaxies ($z \approx 0.5–1.0$) analyzed so far from the LSD Survey (i.e., 0047−285, MG 2016+112, and the three systems discussed in § 2), together with the published linear fits for the FP *M/L* evolution of cluster and field E/S0 galaxies. The effective *M/L* evolution for the five lens galaxies is $d \log (M/L_B)/dz = -0.72 \pm 0.10$; i.e., E/S0 galaxies were on average brighter at $z = 1$ by 1.82 ± 0.26 mag in the rest-frame *B* band. This number assumes that the intercept of the local FP of field E/S0 galaxies is the same as that of Coma Cluster galaxies, consistent with the very small environmental dependence of the intercept in the local universe [less than 0.1 dex in $\log (M/L_B)$; e.g., van Dokkum et al. 2001; Bernardi et al. 2003]. For completeness, we mention that if the local intercept is allowed to vary, the best-fit values are $d \log (M/L_B)/dz = -0.42 \pm 0.19$ and $\gamma_{\rm FP,lenses} - \gamma_{\rm FP,Coma} = -0.23 \pm 0.14$, where the error bars are large because of the small number of points and the limited redshift range covered by our sample. The full LSD sample, including the low-redshift objects, is needed to simultaneously fit for the local
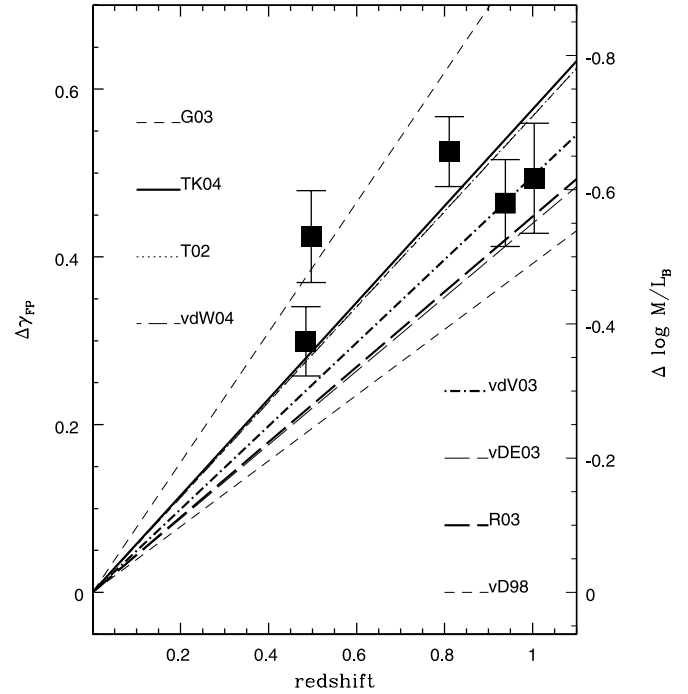
intercept and its redshift evolution. In this paper we therefore restrict our analysis to the fit of the redshift evolution. We note that lens galaxies are not located in rich clusters and therefore this sample of lens galaxies is more similar to the samples of *field* E/S0s than those of cluster E/S0s.

In terms of the passive evolution of a single stellar population, this corresponds to a relatively recent epoch of formation $z_{\rm ssp} \sim 1.3$ (for a Bruzual & Charlot GISSEL96 population synthesis model with Salpeter initial mass function and solar metallicity; see T01a and T02 for more details), i.e., somewhat younger stars than typically observed for massive cluster E/S0 galaxies [for which $d \log (M/L_B)/dz = -0.49 \pm 0.05$ corresponding to $z_{\rm ssp} \sim 2$; van Dokkum et al. 1998]. However, this evolutionary rate is also consistent with a scenario where most of the stars in field E/S0 galaxies are old and formed at $z > 2$ (for example, MG 2016 was found to have a star formation redshift of ~ 2; KT02), and the relatively fast evolution is driven by secondary bursts of star formation contributing $\sim 10\%$ to the stellar mass between $z \sim 1$ and today. The latter scenario appears to be favored on the grounds of three independent lines of evidence: (1) early-type galaxies are present in the field in significant numbers out to well beyond $z \sim 1$, inconsistent with a sudden creation at $z \sim 1.3$ (e.g., Treu & Stiavelli 1999; Chen et al. 2003; Fukugita et al. 2004; Glazebrook et al. 2004); (2) recent star formation in a fraction of high-*z* E/S0 galaxies is detected from alternative diagnostics, such as colors (e.g., Menanteau et al. 2001; van de Ven et al. 2003, hereafter vdV03) and absorption- and emission-line diagnostics (e.g., T02; Willis et al. 2002; van

Dokkum & Ellis 2003); and (3) a "frosting" of younger stars is found by comparing detailed stellar population models with the spectra of local field E/S0s (e.g., Trager et al. 2000).

The faster evolution of field versus cluster E/S0 galaxies is qualitatively in agreement with the prediction of hierarchical models (Kauffmann 1996; Diaferio et al. 2001; Benson et al. 2002); however, *quantitatively* the difference is smaller than predicted (see Treu 2004 for a recent review and discussion of this comparison from a more general point of view).

3.2. *Discussion and Comparison with Previous Work*

Our measurement is in good agreement with the results (using direct measurements of the central stellar velocity dispersion, σ) published by T02, who find $d \log (M/L_B)/dz = -0.71^{+0.11}_{-0.16}$, and by van der Wel et al. (2004), who find -0.71 ± 0.20. In contrast, van Dokkum & Ellis (2003) find a marginally slower evolution $d \log (M/L_B)/dz = -0.55 \pm 0.05$, while Gebhardt et al. (2003) measure a much faster evolution, i.e., 2.4 mag to $z = 1$, corresponding to a value of $d \log (M/L_B)/dz \approx -0.96$. At face value these results appear inconsistent at the 1–2 σ level. Assuming that mutually consistent measurement techniques have been adopted,[11] the differences could arise for a variety of reasons.

A first possible explanation is that the various samples cannot be directly compared because of subtle differences between the morphological classification schemes. Indeed, van Dokkum & Ellis (2003) found that the two overluminous E/S0 galaxies in their sample of nine showed asymmetric features in the Hubble Deep Field images. A larger sample of objects with deep imaging is necessary to quantify this effect.

Second, luminosity-selected samples favor overluminous objects and are therefore biased toward faster evolution. The extent of the bias depends on the intrinsic scatter of the FP and on the magnitude limit. It can be corrected by taking into account the selection procedure in the analysis (T01a; T02). To further complicate matters, the evolutionary rate could be a function of mass, with more massive galaxies evolving slower than less massive ones (e.g., van der Wel et al. 2004; note also that H1543, the lens galaxy with the largest offset from the local FP, is also the least massive one), resulting in a change of the FP slopes with redshift. In this case, the mean evolutionary rate would be a function of the mass range of the sample (T02). Unfortunately, luminosity selection could also mimic a change in the slope because less massive galaxies would make the cut only if they are overluminous (Kelson et al. 2000). We note here that a lens sample, although in principle mass selected, could suffer from the same kind of bias because of the effective magnitude limit imposed by spectroscopic follow-up. The statistical analysis of larger samples of lens galaxies is essential to determine simultaneously the evolution of the intercept, slopes, and scatter of the FP, correcting for selection effects.

A third possible explanation is cosmic variance. If indeed the secondary burst scenario is correct, at any given time the majority of E/S0 galaxies would be observed to follow a quiescent passive evolution path in the FP space, while a fraction of E/S0 galaxies would be observed within 1–2 Gyr after the secondary burst, while overluminous. The fraction of overluminous E/S0 galaxies would depend on the duty cycle of secondary bursts. If, for example, ~10% of the stellar mass

is formed in each secondary burst, each galaxy undergoes one secondary burst between $z = 1$ and 0, and the bursts are detectable for 2 Gyr, then one-quarter of the E/S0 galaxies between $0 < z < 1$ would be overluminous. Therefore, only a handful of overluminous galaxies would be observed in the current samples of galaxies and small number statistics could be dominating the uncertainties.

Following Kochanek et al. (2000), both Rusin et al. (2003b, hereafter R03b) and vdV03 recently used image separations (or Einstein radii) of arcsecond-scale strong lens systems to estimate the central velocity dispersion of E/S0 lens galaxies and construct an FP. The key assumption is that lens galaxies have isothermal mass profiles (i.e., $\rho \propto r^{-2}$) and therefore the central velocity dispersion can be obtained directly from the image separation with the assumption that $\sigma \approx \sigma_{\rm SIE}$ (see Kochanek et al. 2000). Under this assumption, R03b find $d \log (M/L_B)/dz = -0.56 \pm 0.04$, and vdV03, using the photometry and image separations from R03b, find $d \log (M/L_B)/dz = -0.62 \pm 0.13$, using larger errors and a different weighting scheme. The fact that these estimates are so close to the direct measurements discussed above is indeed remarkable. Not only do many of the above arguments, related to selection effects and small sample statistics, also apply to lens galaxy samples, departures from isothermal mass profiles, or effects such as a mass-sheet degeneracy, introduce additional sources of uncertainty. In other words, the relatively good agreement between the direct and indirect methods tells us that the isothermal approximation is probably not dramatically wrong.

In the next sections, via a joint lensing and dynamics analysis, we further examine the accuracy of this approximation. However, before we proceed to the full analysis, we can gain some insight by looking at the three objects in our sample that are also in R03b and vdV03: 0047, H1417, and MG 2016. The offset from the local FP is in agreement within the errors for 0047 and MG 2016 (see also R03b), while for H1417 we measure ~0.1 dex more evolution for $\log (M/L_B)$. The difference is entirely due to the difference between our *direct* measurement of the stellar velocity dispersion ($\sigma = 224 \pm 15$ km s^{-1}) and the velocity dispersion inferred from the image separation (~290 km s^{-1}; vdV03; R03b; next section). Hence, in at least one case, the image separation underestimates the stellar velocity dispersion. As shown in § 7, this is the case in three out of five lens systems in our sample.

4. GRAVITATIONAL LENS MODELS

As in previous work on LSD lens systems (KT), we model the three systems (C0302, H1417, and H1543) with a singular isothermal ellipsoid (SIE) mass distribution:

$$\kappa_{\rm SIE}(x, y) = \frac{b_l \sqrt{q}}{2\sqrt{y'^2 + q^2 x'^2}}, \qquad (2)$$

with $b_l = 4\pi(\sigma_{\rm SIE}/c)^2 (D_d D_{ds}/D_s)$ and the major axis aligned north-south (Kormann et al. 1994). We define (x', y') (in rad) in equation (2) as the frame centered on the lens (x_l, y_l) and aligned with the P.A. of the lens θ_l. Because the mass enclosed by the elliptical critical curve is independent of the flattening of the mass distribution $q = (b/a)$, we find that $R_{\rm Einst} = D_d b_l$ corresponds to the equivalent singular isothermal sphere (SIS) Einstein radius. The equivalent SIS mass ($M_{\rm Einst}$) is that enclosed by the critical curve. Both $R_{\rm Einst}$ and $M_{\rm Einst}$ are

---

[11] As suggested by the good agreement between the FP parameters measured by different groups; see § 2.2 and Gebhardt et al. (2003).

TABLE 4
Astrometry of the Lens System H1417

Object	ΔR.A.	ΔDecl.	r
A....................................	-1.266 ± 0.006	-1.139 ± 0.006	0.81 ± 0.16
B....................................	-0.843 ± 0.006	$+0.918 \pm 0.006$	0.65 ± 0.08
C....................................	$+0.792 \pm 0.006$	$+1.321 \pm 0.006$	1.00 ± 0.13
D....................................	$+0.814 \pm 0.006$	-0.803 ± 0.006	0.57 ± 0.18
G....................................	$+0.000 \pm 0.004$	$+0.000 \pm 0.004$	...

Note.—The column r lists the F814W flux ratios of the multiple images normalized to image C, taken from the CASTLES Web database.

needed in the joint lensing and dynamical analysis. We refer to KT03 for additional discussion of the models. We note that the enclosed mass $M_{\rm Einst}$ is nearly independent of the choice of mass model and depends predominantly on the monopole of the lens potential (Kochanek 1991). We also allow for an external shear with strength $\gamma_{\rm ext}$ and P.A. $\theta_{\rm ext}$, corresponding to the potential $\psi_{\rm ext}(x, y) = -R^2(\gamma_{\rm ext}/2) \cos 2(\theta - \theta_{\rm ext})$, where we define $R^2 = (x - x_l)^2 + (y - y_l)^2$ to be the square of the distance to the lens center. We emphasize that our lens model is fully two-dimensional and therefore takes correctly into account deviations from circular symmetry (e.g., Sand et al. 2004; Dalal & Keeton 2003; Bartelmann & Meneghetti 2004).

Only H1417 has well-defined lensed images and fluxes (Fig. 1). For this lens system, previously modeled by Knudson et al. (2001), we use the "traditional" modeling technique, in which the source is represented by a single point in the source plane with a given flux, which is magnified and mapped onto the lensed images in the image plane. We use the code described in K03. To model the extended images of C0302 and H1543, we implemented a code (see Appendices A, B, and C) that incorporates techniques described in W96 and WD03, allowing the full use of all the lensing information contained in the images.

4.1. HST 14176+5226

We first model the lens system with an SIE mass distribution and external shear only. The lens strength (b_l), centroid (x_l, y_l), ellipticity (q), and P.A. (θ_l) are free parameters, as well as the external shear, the source position, and its flux. The lens centroid and P.A. are further constrained by the observational priors given in Tables 1 and 4. The best model has $\chi^2/\mathrm{NDF} = 38$ for $\mathrm{NDF} = 4$, using the image constraints in Table 4, and is clearly not satisfactory.[12]

The next order of observable complexity that can be introduced is a linear gradient in the surface density of the mass model and has a potential of $\psi_g(x, y) = (R^3/4) |\nabla \kappa_g| \cos (\theta - \theta_g)$. This gradient can be the result of an external perturber (e.g., group or cluster) but also an internal asymmetry of the lens (e.g., $M = 1$ mode). We assume $\kappa_g = 0$ for a line through the lens centroid, i.e., $R^2 = (x - x_l)^2 + (y - y_l)^2$, such that the convergence gradient adds no mass inside a symmetric aperture on the lens centroid (x_l, y_l). This adds two more free parameters (i.e., $|\nabla \kappa_g|$ and θ_g). The best model in this case has $\chi^2/\mathrm{NDF} = 3.2$ for $\mathrm{NDF} = 2$, which is considerably better than a model without a convergence gradient. We feel

that adding more free parameters is no longer justified, since both χ^2 and NDF are small.

We notice that the gradient points in the direction of the major axis of the SIE mass distribution and *not* in the external shear direction. The direction of the gradient and the major axis of the SIE coincide within $11°$ and are consistent at the $2.5\ \sigma$ level. We also notice that the agreement improves to within $\sim 9°$ if the major axis is not constrained by a prior. To further examine this possible alignment, we also tested the SIE plus shear and gradient model on PG 1115+080 (a model similar to Treu & Koopmans 2002b, hereafter TK02b). We find that for the best model, the P.A. of the gradient and external shear agree, both pointing to the confirmed external perturber, which is a compact group $\sim 13''$ from the lens (Kundič et al. 1997a). In the case of H1417, however, there exists no obvious group or cluster in the $\sim 1'$ field around the lens system,[13] and the gradient and shear P.A. differ at the $12\ \sigma$ level, nor are any of the galaxies around the lens massive enough to account for the observed gradient of $|\nabla \kappa_g| = 0.102 \pm 0.015$. A simple argument based on an SIS perturber shows that one would expect its distance from H1417 to be related to the Einstein radius of the perturber by $(R/R_{\rm Einst})^2 \approx 1/(2|\nabla \kappa_g|)$, or $R \approx 2.2 R_{\rm Einst}$. A massive cluster with $R_{\rm Einst} = 30''$ would still be detectable in the field around the lens. A single massive galaxy with $R_{\rm Einst} = 2''$ would be within $R \approx 5''$ from the lens, in the direction of increasing κ_g, i.e., $\theta_g \approx 200°$. Neither is obviously found. We therefore conclude that the detected gradient is most likely associated with an asymmetry in the lens mass distribution. A significant gradient is also required for models with density slopes other than isothermal.

The best SIE model is shown in Figure 5, and all model parameters are listed in Table 4. The equivalent SIS velocity dispersion, mass, and Einstein radius of the lens are $\sigma_{\rm SIE} = 290 \pm 8$ km s^{-1}, $M_{\rm Einst} = (70.8 \pm 7.6) \times 10^{10}\ M_{\odot}$, and $R_{\rm Einst} = 11.4 \pm 0.6$ kpc ($1''41 \pm 0''08$), respectively (68% CL errors). Our derived Einstein radius ($1''41$) agrees to within $\leq 0''01$ with that derived by R03b. As noted, the gradient adds no mass.

To further test the robustness of the enclosed mass measurement, we examine three more sources of uncertainty. First, we find that the mass enclosed by a circular aperture with $1''41$ radius gives a mass that is only 2.0% lower than our best estimate of the mass within the elliptical critical curve. Second, the best χ^2 models with density slopes that are 40% steeper/shallower than isothermal have enclosed masses different by only $-2.0\%/+1.3\%$. Third, if κ_g is caused by an external perturber, a mass sheet ($\kappa_{\rm sheet}$) must be associated with it, since truly negative values of κ_g are not allowed. An estimate of the external convergence can be obtained from the external shear, assuming an isothermal mass distribution, i.e., $\kappa_{\rm sheet} \sim \gamma_{\rm ext}$. If we set $\kappa_{\rm sheet} = \gamma_{\rm ext}$, we find that the velocity dispersion, enclosed mass, and Einstein radius decrease by 2.5%, 10%, and 5%, respectively. However, in the absence of any evidence for external perturbers that could result in a nonlocal convergence, we conclude that the mass measurement is robust and reliable and does not introduce a bias in the final lensing plus dynamics analysis (§ 6). To account for most of the uncertainties, we assume a total 1 σ error of 10% on the enclosed mass.

---

[12] The χ^2 value is dominated by the lens position ($\chi_l^2 = 84$) and the lensed image positions ($\chi_i^2 = 65$). The flux ratios contribute only $\chi_r^2 = 2$. Since the images are somewhat extended (see Fig. 1) and have no apparent compact structure that could be affected by stars (i.e., microlensing) or substructure, one would not expect significant flux ratio anomalies.

[13] Although an overdensity of galaxies at $z \sim 0.8$ in the Groth Strip might be present (Koo et al. 1996; Im et al. 2002).
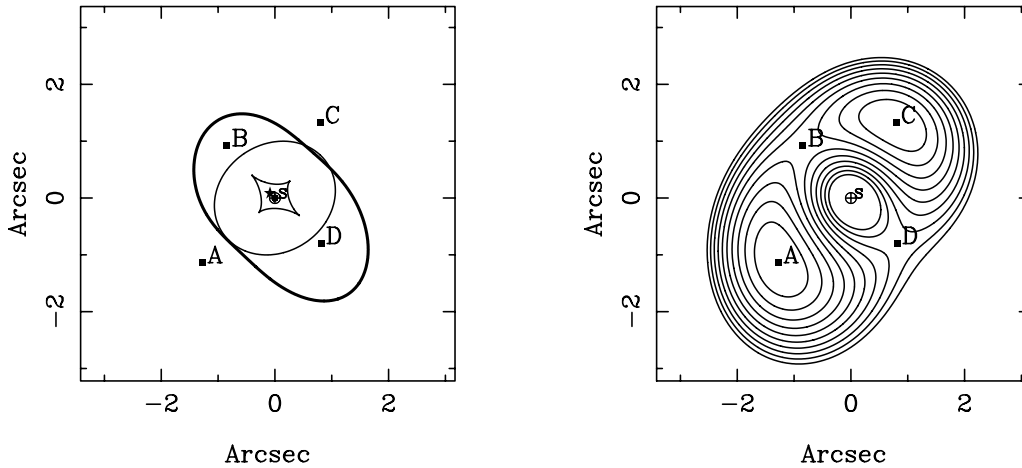
FIG. 5.—Best-fitting SIE lens model of H1417. The left panel shows the position of the lens (*filled circle*) and the multiple images (*filled squares*) on the image plane, together with the critical line (*thick solid line*). The caustics (*thin lines*) and source position (*filled star*) on the source plane are also shown. The right panel shows the time delay surface with constant time-delay contours increasing from 0.0 (at A) to 83 days in steps of 8.3 days.

4.2. *CFRS 03.1077*

The lensed arc and counterimage in the system C0302 (Crampton et al. 2002; Hammer et al. 1995; Lilly et al. 1995) do not have enough structure to allow a simple one-to-one mapping between them. To determine the total enclosed mass, we implemented a lens code that combines elements from W96 and WD03 and that can model extended lensed images on a grid (i.e., CCD image). In Appendices A, B, and C we outline the general features of the code and where it differs from W96 and WD03.

In the discovery paper, Crampton et al. (2002) modeled the lens using a nonsingular isothermal ellipsoid (NIE) mass model with nonzero core radius. They find a good fit to the arc and counterimage, using an axisymmetric source model just outside the cusp. A high velocity dispersion of 387 ± 5 km s^{-1} is inferred from their lens model, leading to the conclusion that the lens galaxy is as faint as present-day elliptical galaxies of similar central velocity dispersion and thus shows no sign of passive evolution. Since there are several dwarflike galaxies near the main lens galaxy (Fig. 1), possibly indicating the presence of a small group, the apparent underluminous nature of the lens galaxy might be the result of an increased dark matter fraction inside the Einstein radius from a group halo. Groups have been found near a number of other lens systems; hence, they might not be uncommon and should be accounted for in lens models where necessary (e.g., Lehar et al. 1997; Kundič et al. 1997a, 1997b; Tonry 1998; Tonry & Kochanek 1999, 2000; Blandford et al. 2001; Keeton et al. 2000; Fassnacht & Lubin 2002; Johnston et al. 2003).

In our model, we associate the mass centroid with the light centroid of the lens galaxy and model its mass distribution as an SIE with the lens strength, P.A., and ellipticity as free parameters. The P.A. is left free (as opposed to H1417) because the nearby companions (Fig. 1) could introduce a difference between the luminous and mass P.A.; external shear is added.

The source grid is 39×39 pixels (40 mas pixel^{-1}). Pixels in the image plane within 1 σ of the noise level are clipped and do not participate in the determination of the best model (clipping at 2–3 σ results in a very similar model). Image-plane pixels that map outside the source grid and vice versa are masked. We minimize the reduced χ^2, to properly account

for the variable number of participating source and image-grid pixels. We use an appropriate PSF generated with Tiny Tim. A value of $\lambda = 0.02$ for the smoothing parameter (see Appendices A, B, and C) leads to $\chi^2/\mathrm{NDF} \approx 1$.

Since the external shear is large, we find a strong degeneracy between the lens galaxy ellipticity and P.A. and the external shear. The constraint on $q = (b/a)$ is therefore relatively weak. Since the external shear appears to align with the P.A. of the light distribution, not the mass model, we suspect that some of the external shear is in fact "internal" shear due to the stellar component and that the lens galaxy is embedded in a larger misaligned structure (e.g., a group halo). The presence of at least five small dwarfs around C0320 would support this (Fig. 1). These degeneracies, however, have negligible effect on the determination of enclosed mass within the images.

The best SIE plus shear model is shown in the left panels of Figure 6, and the mass model parameters are listed in Table 5. We have refrained from calculating precise formal errors, as for H1417, which is extremely difficult given the variability of NDF (i.e., the number of participating pixels) and the free choice of source-pixel size and λ. It is also computationally very expensive *if* the mass model is not fixed (see WD03 for the case when it *is* fixed). We plan to further refine the code (currently written in IDL), increase its speed, and allow for a full nonlinear error analysis. Nevertheless, a conservative upper limit of $\lesssim 5\%$ can be set on the 1 σ error on the Einstein radius, being roughly the width of the arc divided by its distance to the lens centroid. The equivalent SIS velocity dispersion, mass, and Einstein radius of the lens in C0302 from the best model then become $\sigma_{\mathrm{SIE}} = 294 \pm 8$ km s^{-1}, $M_{\mathrm{Einst}} = (67.0 \pm 6.7) \times 10^{10}$ $M_{\odot}$, and $R_{\mathrm{Einst}} = 10.6 \pm 0.5$ kpc (1″24 $\pm$ 0″06), respectively.

The dominant component of the source straddles the cusp on the outside and appears compact and relatively symmetric with possibly some indication of extended structure around it. The shape and position in the source plane are similar to those found by Crampton et al. (2002), even though their stellar velocity dispersion, from a nonsingular model, is much higher than our SIE velocity dispersion. This appears to be a result of the use of a nonzero core radius and their definition of σ, which increases with increasing core radius (F. Hammer 2003, private communication). We note that our definition of σ_{SIE} is
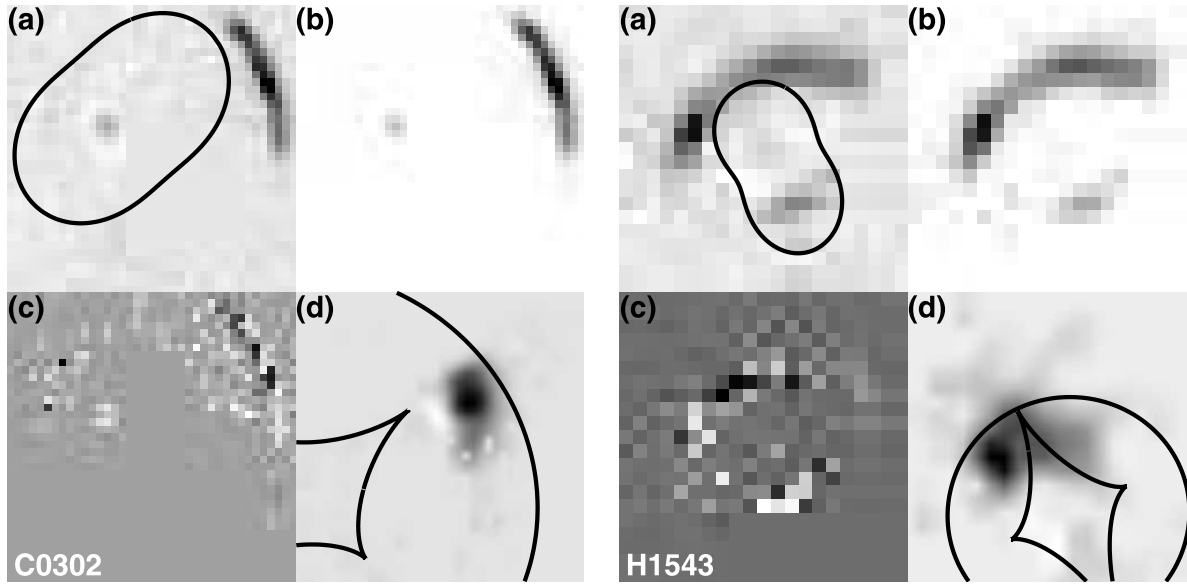
Fig. 6.—Best LENSGRID (§ 4) reconstructions of the extended arcs and counterimages in C0302 (*left*) and H1543 (*right*). (*a*) Original image with lens galaxy subtracted; (*b*) best reconstruction; (*c*) difference between observation and model; (*d*) source in the source plane, regridded and smoothed by a Gaussian with FWHM = $0\rlap{.}''08$ to highlight its structure. The curves are the critical (*upper left*) and caustic (*lower left*) curves.

in accordance with previous work, including that of Kochanek et al. (2000) and R03b.

4.3. *HST 15433+5352*

The modeling of H1543 proceeds very similarly to that of C0302, with the following differences. First and foremost, there are several massive nearby perturbers that have to be accounted for in the model. The strongest is a massive galaxy (G2) approximately $4\rlap{.}''7$ to the east of the lens galaxy (G1) with a measured central stellar velocity dispersion of $\sigma = 263 \pm 11$ km s^{-1}. We model this galaxy as an SIS (eq. [2] with $q = 1.0$) with $\sigma_{\rm SIE} = \sigma$.

Another galaxy (G3) at the same redshift of G1 and G2 was serendipitously detected in the LRIS slit, $18''$ away from G1 on the opposite side of G2. Since H1543 falls near the edge of the WFPC2 field, no *HST* images are available of G3. However, images of the region are available from the Sloan Digital Sky Survey (SDSS) Data Release 1 (Abazajian et al. 2003). A visual inspection of the images shows indeed a galaxy at the location of G3, as well as other galaxies with similar colors

TABLE 5
SIE GRAVITATIONAL LENS MODELS

Parameter	H1417	C0302	H1543
x_l (arcsec)	$-0.001^{+0.004}_{-0.004}$	...	...
y_l (arcsec)	$-0.001^{+0.004}_{-0.004}$	...	...
b_l (arcsec)	$1.41^{+0.10}_{-0.06}$	1.24	0.36
q_l	$0.65^{+0.05}_{-0.06}$	0.83	$\equiv 0.95$
θ_l (deg)	$31.7^{+3.5}_{-4.0}$	-33.4	16.0
$\gamma_{\rm ext}$	$0.12^{+0.01}_{-0.02}$	0.17	0.17
$\theta_{\rm ext}$ (deg)	$66.5^{+3.4}_{-2.1}$	-54.9	71.6
$\nabla\kappa_g$ (arcsec^{-1})	$0.102^{+0.015}_{-0.015}$	...	...
θ_g (deg)	$200.4^{+4.7}_{-5.7}$	...	...

NOTES.—The lens centers of C0302 and H1543 are fixed at the observed galaxy centroids. The sky P.A. values are given.

and luminosities in the vicinity, consistent with the presence of a group (see the discussion on groups for C0302).

Our best SIE plus shear model is shown in Figure 6. Relatively little regularization is needed ($\lambda \sim 0.003$). The source is relatively compact, which lends further credit to the model. As expected from the presence of the nearby aligned perturbers (G2 and group), we find the external shear, $\gamma_{\rm ext} = 0.17$, to be large and dominant over the mass ellipticity of the lens galaxy. To avoid degeneracies between external shear and lens galaxy ellipticity, we therefore restricted ourselves to an SIE mass model with $q = 0.95$ fixed. We also tested SIE plus shear models with varying ellipticities and find no strong differences between their critical and caustic structures, nor between the enclosed mass within the equivalent SIE Einstein radius. The shear P.A. ($\sim 72°$) aligns nearly perfectly with the line between G1, G2, and the compact group ($\sim 67°$), suggesting that the external shear is real and most likely due to the group. The shear of G2 is already accounted for by its SIS mass model.

The equivalent SIS velocity dispersion, mass, and Einstein radius of the lens in H1543 from the best model are $\sigma_{\rm SIE} = 139 \pm 7$ km s^{-1}, $M_{\rm Einst} = (3.4 \pm 0.7) \times 10^{10}\ M_\odot$, and $R_{\rm Einst} = 2.4 \pm 0.4$ kpc ($0\rlap{.}''36 \pm 0\rlap{.}''04$), respectively. As for H1417, we can estimate the mass associated with the external mass distribution from the external shear. If a mass sheet with $\kappa_{\rm sheet} \sim \gamma_{\rm ext} \sim 0.17$ contributed to the image separation, one would overestimate the mass of the galaxy by $\sim 17\%$. To account for this uncertainty, we adopt a conservative error of 20% on $M_{\rm Einst}$, twice that of the other two systems. This range also covers the majority of models, when varying different assumptions in the models (e.g., ellipticity).

We note that if G2 and the group are dynamically associated with the lens galaxy, their dark matter mass halos also contribute to the mass inside the Einstein radius of the lens (G1), affecting both lensing and stellar dynamics. Therefore, one should not regard this as a systematic effect that should be removed like a mass sheet, since this mass truly contributes to

the inner slope of the dark matter halo of the lens galaxy. We discuss this important point in more detail in § 7.

5. THE TWO-COMPONENT MASS MODEL

Following our previous papers (TK02a, KT03), in the lensing plus dynamics analysis, we model the lens galaxies as a superposition of two spherical components, one for the luminous stellar matter and one for the dark matter halo. The luminous mass distribution is described by either a Hernquist (1990)

$$\rho_{\mathrm{lum}}(r) = \frac{M_* r_*}{2\pi r (r + r_*)^3} \tag{3}$$

or a Jaffe (1983) model where M_* is the total stellar mass. For consistency with TK02a we show primarily the results obtained with the Hernquist profile and discuss how they change using a Jaffe profile where relevant. The dark matter halo is modeled as

$$\rho_{\mathrm{DM}}(r) = \frac{\rho_{\mathrm{DM},0} r_b^3}{r^\gamma (r_b^2 + r^2)^{(3-\gamma)/2}}, \tag{4}$$

which closely resembles an NFW profile for $\gamma = 1$ and has the typical asymptotic behavior at large radii found from numerical simulations of dark matter halos $\propto r^{-3}$ (e.g., Ghigna et al. 2000). In accordance with the CDM picture (e.g., Bullock et al. 2001) we expect the break radius r_b to be much larger than the effective and Einstein radii. Therefore, in the following we set $r_b \gg R_{\mathrm{Einst}}$, effectively equivalent to ∞; i.e., we describe the dark matter halo as a simple power law $\rho_{\mathrm{DM}} \propto r^{-\gamma}$ in the region of interest. To further explore the effects of the distribution of mass at large radii, we have done tests with (1) a dark matter halo, as in equation (4), but falling off as r^{-4} at large radii (equivalent to a Hernquist or Jaffe model for $\gamma = 1$ or 2, respectively), and (2) values of r_b as small as $\lesssim R_e$. In all cases we find that the effects on the stellar velocity dispersion due to changes in the break radius and outer slope are negligible if $r_b \gtrsim 3R_e$. In the current ΛCDM models, break radii as small as $r_b \lesssim 3R_e$ are highly unlikely for most galaxies, since R_e is typically only several kiloparsecs. Our approximation of $r_b \to \infty$ is therefore justified, and the resulting constraints on γ can be compared with the inner dark matter mass slope from simulations *after* baryonic collapse (e.g., cooling), which can alter the inner slope of the dark matter halo but much less so the outer slope.

We assume an Osipkov-Merritt (Osipkov 1979; Merritt 1985a, 1985b) parameterization of the anisotropy of the stellar mass distribution or a constant $\beta(r)$ model,

$$\beta(r) = \begin{cases} 1 - \dfrac{\sigma_\theta^2}{\sigma_r^2} = \dfrac{r^2}{r^2 + r_i^2}, & r_i \geq 0, \\ b_{\mathrm{iso}} \in [-1, +1], \end{cases} \tag{5}$$

where σ_θ and σ_r are the tangential and radial components of the velocity dispersion, respectively, and r_i is called the anisotropy radius. Note that $\beta \geq 0$ by definition for the Osipkov-Merrit model, not allowing for tangentially anisotropic models. At infinite radii, Osipkov-Merrit models become completely radial. Although this behavior is not commonly found within the inner regions of E/S0 galaxies probed by observations (e.g., Gerhard et al. 2001; see also

van Albada 1982 and Bertin & Stiavelli 1993 for theoretical grounds), it has little impact in the case considered here, since the pressure tensor only becomes significantly radial well outside the Einstein radius and in projection is significantly downweighted by the rapidly falling luminosity-density profile. To test tangential anisotropy, we also considered models with constant anisotropy $\beta(r) = b_{\mathrm{iso}}$ varying from -1 to $+1$. Whereas for $b_{\mathrm{iso}} = 1 \to 0$ the behavior is very similar to $r_i = 0 \to \infty$, the effect on the inferred mass slope γ' for $\beta = -1$ to 0 is almost negligible (Fig. 7d). We therefore do not consider these models further in detail but only mention them when necessary.

The line-of-sight velocity dispersion is obtained by solving the three-dimensional spherical Jeans equation for the luminous component in the total gravitational potential and computing the luminosity-weighted average along the line of sight (e.g., Binney & Tremaine 1987; Kochanek 1994). We correct for the average seeing during the observations and average the velocity dispersion (weighted by the surface brightness) inside the appropriate rectangular apertures. For completeness, we rescale the model apertures such that their projection on the axisymmetric model is equivalent to their projection on an elliptical galaxy with an axial ratio of b/a. This has minimal effects on the model velocity dispersions—much smaller (i.e., $<1\%$) than the observational errors—since the observed and model dispersion profiles are typically very flat. The uncertainties on seeing, aperture size, and galaxy centering are taken into account as systematic errors in the following discussion. Additional discussion of our mass profiles and dynamical model can be found in TK02a and KT03.

6. A JOINT LENSING AND DYNAMICAL ANALYSIS

We are now in the position to use the measurements derived in §§ 2.1, 2.2, and 4 to constrain the free parameters in our two-component mass models. Surface photometry gives directly $r_* = R_e/1.8153$ for the Hernquist model, assuming that the stellar mass-to-light ratio is constant. The mass enclosed by the Einstein radius is used to obtain $\rho_{\mathrm{DM},0}$, given the other parameters. Likelihood contours of the three remaining parameters (i.e., M_*/L_B, γ, and r_i) are then obtained by comparing the velocity dispersion profiles from the models with the observed ones.

6.1. *The FP as an Additional Constraint*

An additional constraint can be obtained using the offset of the galaxy from the local FP by introducing one further assumption. If the evolution of the effective mass-to-light ratio $\Delta \log (M/L_B)$ is equal to the evolution of the stellar mass-to-light ratio $\Delta \log (M_*/L_B)$, the stellar mass-to-light ratio at redshift z is related to the stellar mass-to-light ratio at $z = 0$ by

$$\log\left(\frac{M_*}{L_B}\right)_z = \log\left(\frac{M_*}{L_B}\right)_0 + \Delta \log\left(\frac{M}{L_B}\right), \tag{6}$$

where the first term on the right-hand side of the equation can be measured for local E/S0 galaxies. Using the local value of $(M_*/L_B)_0 = 7.3 \pm 2.1 \ h_{65} \ M_\odot \ L_{B,\odot}^{-1}$, determined from data by Gerhard et al. (2001) as in TK02a, we infer $M_*/L_B = 1.9 \pm 0.5$, 1.6 ± 0.4, and $2.1 \pm 0.6 \ h_{65} \ M_\odot \ L_{B,\odot}^{-1}$ for the lens galaxies in C0302, H1417, and H1543, respectively. In the next sections we compare these measurements with the *independent* ones obtained from the joint lensing and dynamics analysis, finding a good agreement. Then we use the FP
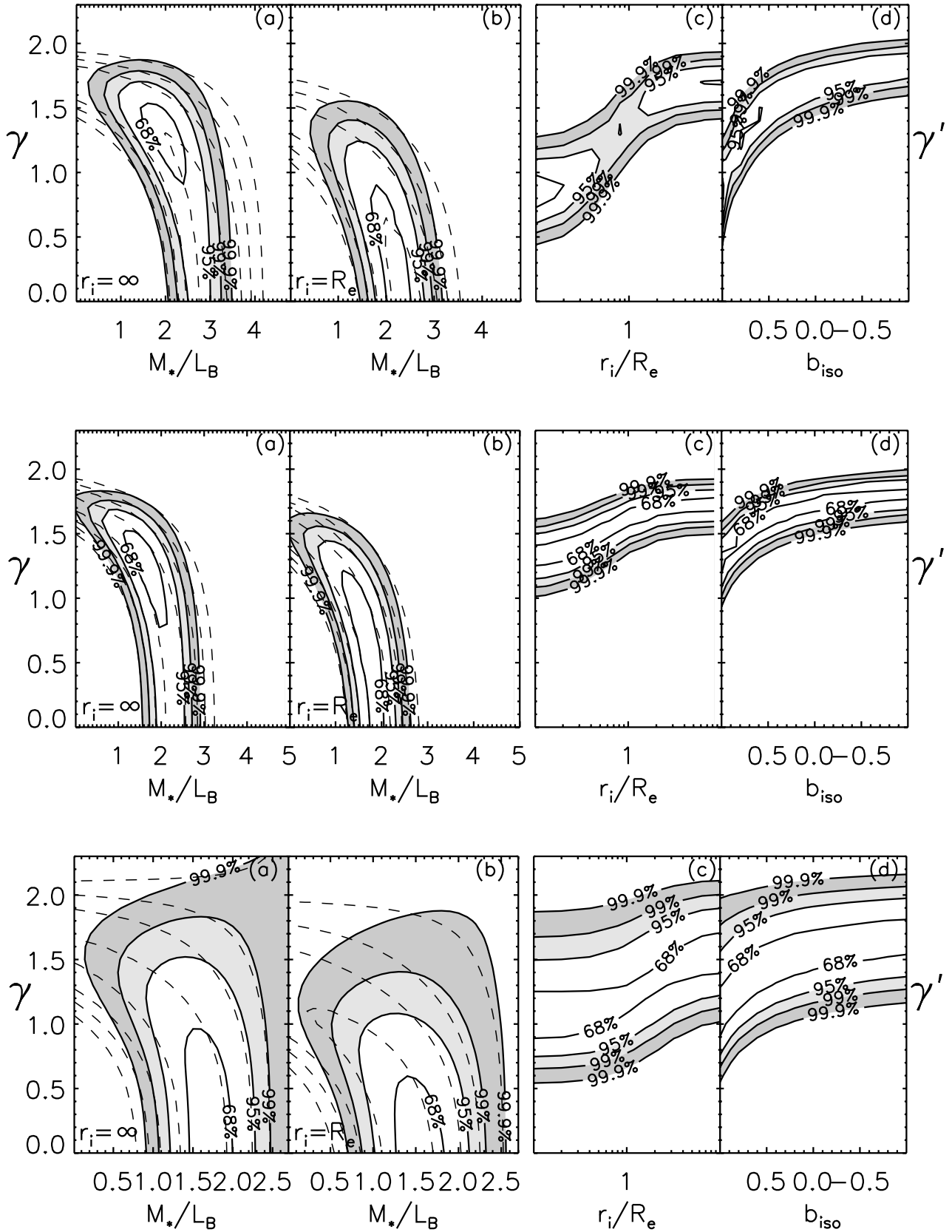
FIG. 7.—Likelihood contours for a joint lensing and dynamical analysis of C0302 (*top*), H1417 (*middle*), and H1543 (*bottom*). (*a*) Contours in the M_*/L_B-γ plane for an isotropic mass model, with (*thick contours*) and without (*dashed contours*) the FP constraints. (*b*) Same as (*a*), but for a radially anisotropic model. (*c*) Contours in the r_i-γ' plane. (*d*) Contours in the γ'-$b_{\rm iso}$ plane. Note that the effective slope γ' changes very little for $b_{\rm iso} = 0 \rightarrow -1$.

TABLE 6
Summary of Lens/Dynamical Model Results I

Galaxy	γ'(iso)	γ'(aniso)	σ_{SIE} (km s^{-1})	f_{SIE}	R_{Einst} (arcsec)	R_e (arcsec)
0047..............	$1.90 \pm 0.05 \pm 0.1$	$1.7 \pm 0.05 \pm 0.10$	252 ± 4	0.91 ± 0.06	1.34 ± 0.01	0.82 ± 0.12
C0302............	$1.70 \pm 0.05 \pm 0.1$	$1.3 \pm 0.10 \pm 0.10$	294 ± 8	0.85 ± 0.06	1.24 ± 0.06	1.60 ± 0.15
H1417............	$1.75 \pm 0.05 \pm 0.1$	$1.7 \pm 0.05 \pm 0.10$	290 ± 8	0.77 ± 0.05	1.41 ± 0.08	1.06 ± 0.08
H1543............	$1.40 \pm 0.20 \pm 0.2$	$1.15 \pm 0.05 \pm 0.10$	139 ± 7	0.83 ± 0.13	0.36 ± 0.04	0.41 ± 0.04
MG 2016........	$2.00 \pm 0.10 \pm 0.1$	$2.0 \pm 0.10 \pm 0.10$	331 ± 10	0.99 ± 0.10	1.56 ± 0.02	0.31 ± 0.06

measurements as a further constraint to the two-component models. However, since this determination relies on a nontrivial assumption (eq. [6]), we present both the results that include this constraint and those that do not.

6.2. *Single Power-Law Mass Models*

Before considering the full two-component models (§ 5), let us first consider a simplified family of models to explore the properties of the total mass distribution, since this is of particular relevance to studies of, for example, the value of H_0 from time delays and also lensing statistics.

As in TK02a and KT03, this family of models consists of a total luminous plus dark matter mass distribution that follows a single power law $\rho_{tot} \propto r^{-\gamma'}$ within the region of interest, where γ' is called the "effective slope." Hence, the luminous mass is assumed to be a trace component in the potential, with $M_*/L_B = 0$. The two remaining free parameters, γ' and r_i, are constrained with the velocity dispersion profile, yielding the results shown in Figure 7c. In Figure 7d, the constant β models are shown, displaying a similar behavior for $b_{iso} \geq 0$, whereas for $b_{iso} < 0$ (tangential anisotropy) almost no effect is seen on the value of γ'.

The best-fit values of γ' depend on the anisotropy of the velocity ellipsoid. As expected, an isotropic velocity ellipsoid ($r_i = \infty$ or $b_{iso} = 0$) leads to a larger value of γ', whereas for the more radial orbital structures ($r_i \rightarrow 0$), a smaller value of γ' is needed. The most likely values of γ' for two representative cases ($r_i = \infty$ and $r_i = R_e$) are listed in Table 6. The corresponding values for MG 2016 and 0047 (TK02a; KT03) are also listed for completeness.

The results are also shown in Figure 8, where we plot γ' as a function of R_{Einst}/R_e. The average slope from the five systems in our sample is $\langle\gamma'\rangle = 1.75 \pm 0.09$ with a large rms of 0.20 (isotropic), or $\langle\gamma'\rangle = 1.57 \pm 0.16$ with an rms of 0.35 (anisotropic). Extremely radial orbits ($r_i \lesssim R_e$) can probably be ruled out, on both observational (e.g., Gerhard et al. 2001) and theoretical grounds, since they would lead to instabilities (Merritt & Aguilar 1985; Stiavelli & Sparke 1991), whereas tangential anisotropy cannot be ruled out; it has a negligible effect (see Fig. 7d).

In the bottom panel of Figure 8 we also show f_{SIE}, i.e., the ratio between the central velocity dispersion and the velocity dispersion of the best-fitting SIE. This number is independent of the choice for the dynamical model. The average is $\langle f_{SIE}\rangle = 0.87 \pm 0.04$ with an rms of 0.08, lower on average than that based on the expectation that $\sigma \approx \sigma_{SIE}$ (Kochanek 1994; Kochanek et al. 2000).

6.3. *Luminous and Dark Matter Mass Decomposition*

Let us now consider the two-component mass models. Once again, we examine the two cases of $r_i = \infty$ and $r_i = R_e$, delineating a conservative range of physical models, and de-

rive likelihood contours in the M_*/L_B-γ plane. The likelihood contours are shown in Figures 7a and 7b. The dashed lines represent the contours obtained without the FP constraint on M_*/L_B, while the solid contours include the FP constraint (§ 6). The main effect of including the FP constraint is to rule out regions with low stellar mass-to-light ratios. In general, the shape of the contours is well understood: the outer luminous component is on average steeper than the dark matter component and therefore smaller values of M_*/L_B require larger values of γ, to compensate and produce a total mass profile as steep as required by the kinematic data. Increasing the radial anisotropy implies a more shallow total mass profile and therefore a smaller value of γ.

In this subsection we discuss constraints on the amount of dark matter within the Einstein radius, through measurements of the total and stellar mass-to-light ratio. In § 6.4 we use these values to determine the cosmic evolution of the stellar mass-to-light ratio and hence the star formation history of E/S0 galaxies. In light of these two goals we determine the fraction
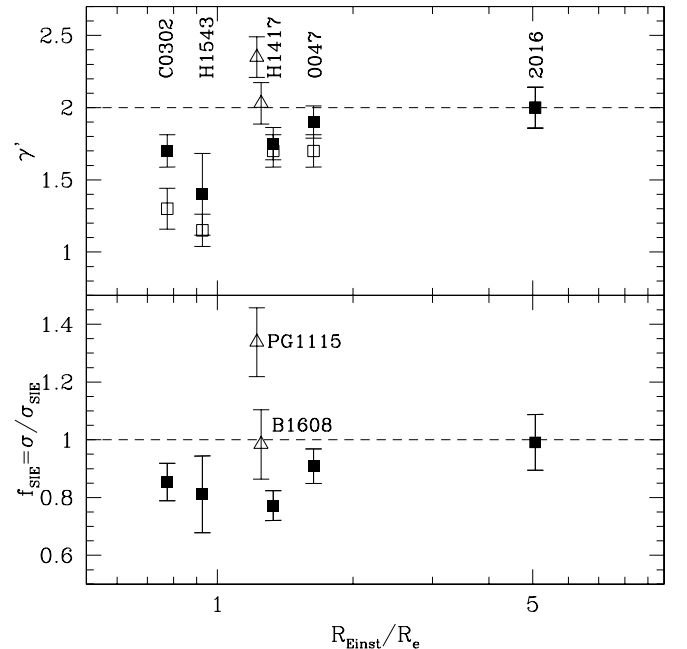

Fig. 8.—*Top*: Effective slope as a function of the ratio between the Einstein radius and the effective radius; filled symbols are obtained for isotropic models ($r_i = \infty$), open symbols for radially anisotropic models ($r_i = R_e$). *Bottom*: Ratio between central velocity dispersion (σ) and velocity dispersion of the best-fitting SIE model as a function of the ratio between the Einstein radius and the effective radius. The horizontal dashed lines represent the expected values for isothermal lens models. The measured values (isotropic models only) for PG 1115 (TK02b) and B1608 (K03)—not included in the LSD sample—are also shown for completeness by open triangles. See §§ 6 and 7 for discussion.

TABLE 7
SUMMARY OF LENS/DYNAMICAL MODEL RESULTS II

Galaxy	M_E $(10^{10}\, M_\odot)$	$(M_{tot}/L_B)_{<R_E}$ $(M_\odot\, L_{B,\odot}^{-1})$	$(M_*/L_B)_{iso}^{ld+FP}$ $(M_\odot\, L_{B,\odot}^{-1})$	$(M_*/L_B)_{iso}^{ld}$ $(M_\odot\, L_{B,\odot}^{-1})$	$f_{DM}^{ld+FP}(iso)$ $(<R_{Einst})$	$f_{DM}^{ld}(iso)$ $(<R_{Einst})$
0047...............	40.6 ± 2.0	5.4 ± 0.5	$3.0^{+0.3}_{-0.6}$	$3.0^{+0.4}_{-1.1}$	$0.44^{+0.11}_{-0.14}$	$0.44^{+0.12}_{-0.22}$
C0302.............	67.0 ± 6.7	4.8 ± 0.5	$2.2^{+0.5}_{-0.5}$	$2.8^{+0.7}_{-0.8}$	$0.54^{+0.15}_{-0.15}$	$0.42^{+0.18}_{-0.20}$
H1417.............	70.6 ± 7.0	5.0 ± 0.5	$1.9^{+0.1}_{-0.2}$	$2.1^{+0.3}_{-0.2}$	$0.62^{+0.10}_{-0.11}$	$0.58^{+0.12}_{-0.11}$
H1543.............	3.4 ± 0.7	2.7 ± 0.5	$1.7^{+0.3}_{-0.4}$	$1.5^{+0.4}_{-0.7}$	$0.37^{+0.22}_{-0.24}$	$0.44^{+0.24}_{-0.32}$
2016...............	110.0 ± 11.0	8.0 ± 0.8	$2.2^{+0.3}_{-0.3}$	$2.5^{+0.3}_{-0.4}$	$0.72^{+0.11}_{-0.10}$	$0.69^{+0.11}_{-0.11}$

NOTE.—The mass-to-light ratio is marginalized over $\gamma > 0$.

of dark matter marginalizing the likelihood contours shown in Figure 7 over γ in two ways: (1) including the FP constraint as a prior, to obtain the most precise measurement of M_*/L_B; and (2) not including the FP constraint, to obtain an independent measurement of the cosmic evolution of M_*/L_B. The results are listed in Table 7. The 68% confidence limits, around the maximum likelihood value, are uniquely determined from the probability distribution function of M_*/L_B (after marginalizing over γ) by the two values of M_*/L_B that have *equal* probability densities and enclose 0.68 of the probability. Since for low values of M_*/L_B the probability density as a function of γ is only large for a small range around $\gamma \sim 2$, it is nearly constant over a large range of γ for $M_*/L_B \sim 2-3$ (Fig. 7). Hence, after marginalization, M_*/L_B has a clearly defined maximum likelihood value and 68% confidence limits.

The total mass-to-light ratio enclosed within the Einstein radius $(M_{tot}/L_B)(<R_{Einst})$ is also listed in Table 7 for comparison. Note that $(M_{tot}/L_B)(<R_{Einst})$ is considerably higher than the limit on M_*/L_B for all five E/S0 galaxies, implying that the galaxies cannot be described by a constant mass-to-light ratio model. Hence, the presence of a mass component spatially more extended than the luminous component is required. We identify this component with the dark matter halo. Quantitatively, we find that for all five E/S0 galaxies (including MG 2016 and 0047), the "no dark matter halo" scenario is excluded at the greater than 99% CL. In other words, a constant mass-to-light ratio model is too steep to satisfy simultaneously the lensing and dynamical constraints and can therefore be ruled out at the 99% CL.

Finally, we note here that M_*/L_B and $(M_{tot}/L_B)(<R_{Einst})$ are correlated through L_B, which is only a scaling factor, useful for the physical interpretation, but irrelevant for the lensing plus dynamical analysis. Thus, it is preferable to express our results in terms of the fraction of dark matter $f_{DM} = (1 - M_*/M_{tot})$, or equivalently in terms of the fraction of luminous matter $f_* = 1 - f_{DM}$. In the isotropic case, the range of dark matter mass fractions inside the Einstein radius is $f_{DM}(<R_{Einst}) = 0.37-0.72$. Translating this into a mass fraction inside R_e is slightly model dependent. However, for $\gamma = 0-1$, the range of dark matter mass fractions is $f_{DM}(<R_e) = 0.15-0.65$, with at most a 10% change (both ways) in the value of f_{DM} between $\gamma = 1$ and 0. This confirms our conclusion that all five E/S0 lens galaxies at $z \approx 0.5-1$ have massive dark matter halos, even well inside the luminous component. Note that these values for the dark matter fraction are significantly higher than the limits obtained from lensing statistics for adiabatically contracted lenses, $f_{DM}(<R_e) < 33\%$ (95% CL; Keeton 2001).

6.4. The Evolution of M_*/L_B from Lensing and Dynamics

The sample of E/S0 lens galaxies reaches a large enough redshift to afford a direct measurement of the evolution of the

stellar populations of E/S0 without including any constraint from the FP. In Figure 9 we have plotted M_*/L_B (Table 7) as a function of redshift. The stellar mass-to-light ratios of E/S0 galaxies at $z \approx 0.5-1.0$ are significantly smaller than in the local universe (on average 2.3 ± 0.6 vs. $7.3 \pm 2.1\, M_\odot\, L_{B,\odot}^{-1}$), implying considerable aging of the stellar populations in the last 4–8 Gyr.

In Figure 9 we also compare our direct lensing plus dynamics measurement of the stellar mass-to-light ratio (Table 7) with the indirect measurement obtained from the evolution of the FP of field E/S0 galaxies (T02). The agreement is very good, consistent with a scenario of pure luminosity evolution of E/S0 galaxies from $z \sim 1$ to today. This measurement rules out scenarios predicting strong evolution of the internal structure of E/S0 galaxies with redshift, where the virial coefficient relating $\sigma^2 R_e$ to the stellar mass would change significantly with cosmic time.

If we use the value of $(M_*/L_B)_{iso}^{ld}$ from Table 7 to determine the evolution of the stellar mass-to-light ratio with redshift, we find that the average evolution is $\langle d\log(M/L_B)/dz\rangle = -0.75 \pm 0.17$, in good agreement with the results from § 3.1, which gave
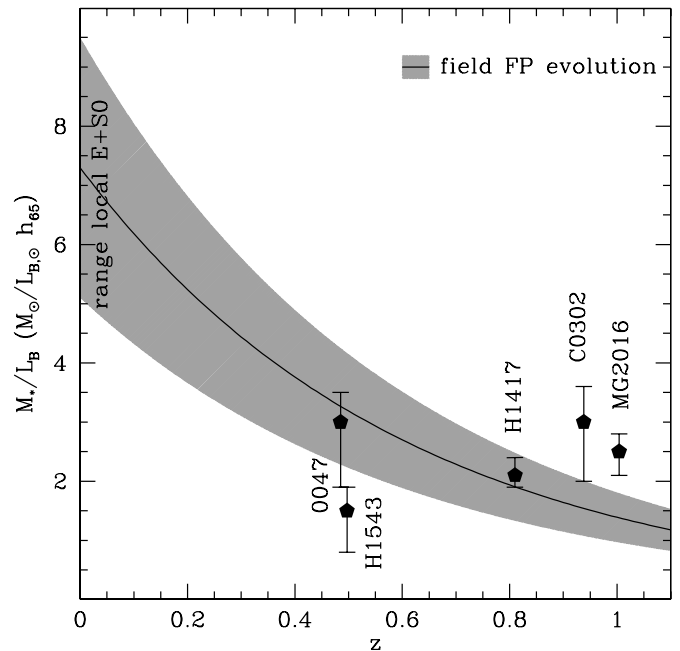

FIG. 9.—Cosmic evolution of the stellar mass-to-light ratio (for an isotropic velocity ellipsoid, $r_i = \infty$). The filled pentagons are the results from the joint lensing and dynamics analysis, whereas the shaded region is the independent measurement via the FP from T02. We emphasize that the latter is not based on lens galaxies and the former not on the FP measurements of M_*/L_B from the five lenses as shown in Fig. 4.
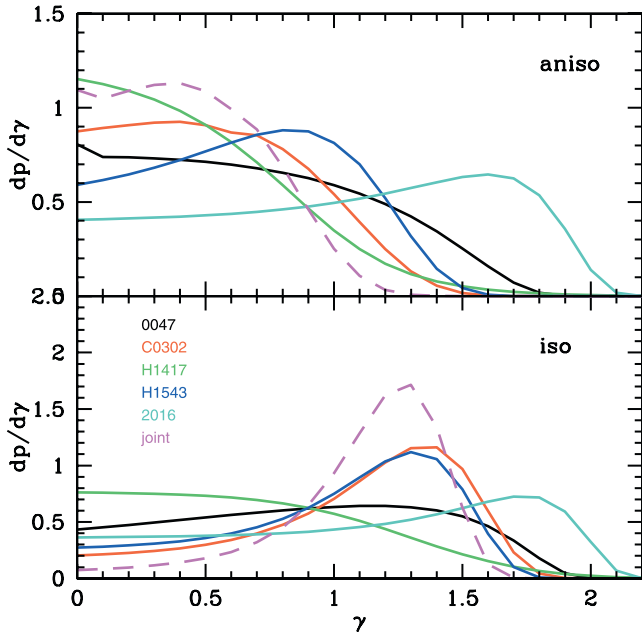
FIG. 10.—Posterior distribution functions for γ for the individual lenses and the joint probability. The case for isotropic orbits is shown in the bottom panel, while the case for radially anisotropic orbits is shown in the top panel.

$d \log (M/L_B)/dz = -0.72 \pm 0.10$ based on the FP. A disagreement between the two independent results would have implied that either the FP is not a good method to derive M_*/L_B evolution or that our lensing plus dynamical analysis is faulty.

6.5. The Inner Slope of the Dark Matter Halos

Since the values of M_*/L_B agree between determinations from the FP and lensing plus dynamics, we can feel confident that their measurements can be combined, as shown by the solid lines in Figures 7a and 7b. The posterior probability distribution functions of γ—marginalized over M_*/L_B, including the FP constraint—for the five lenses are shown by solid colored lines in Figure 10.

For individual lenses these posterior probability distribution functions imply upper limits on γ between ~ 1 and ~ 1.5, i.e., consistent with the inner cusps predicted by cosmological simulations, if the collapse of baryons to form stars did not significantly steepen the dark matter halo (see TK02a; KT02; see also Loeb & Peebles 2003; Sand et al. 2002, 2004; El-Zant et al. 2004; Nipoti et al. 2004). Somewhat tighter confidence limits are obtained when combining the measurements (Fig. 10, dashed line): $0.97 < \gamma < 1.46$ or most likely $\gamma = 1.3^{+0.2}_{-0.4}$ (isotropic) or $0 < \gamma < 0.62$ (anisotropic) at 68% CL and $0.39 < \gamma < 1.59$ (isotropic) or $0 < \gamma < 1.26$ (anisotropic) at 95% CL. In conclusion, the slope of the dark matter halos is definitely flatter than isothermal and ranges between the value predicted by numerical simulations and zero, depending on anisotropy. Requiring consistency with numerical simulations implies that (1) significant radially anisotropic models (i.e., $r_i \approx R_e$) are ruled out and (2) dark matter halos do not significantly steepen during baryonic collapse. More stringent statements cannot be made at this stage because uncertainties related to the orbital properties of the stars dominate the error budget.[14]

7. THE HOMOGENEITY OF EARLY-TYPE GALAXIES

Now that we have homogeneously analyzed a sample of five lenses at $z \approx 0.5-1.0$, we can start to look into the general properties of the E/S0 lens galaxies.[15]

7.1. Are E/S0 Galaxies Isothermal?

The first important question that we want to discuss is the average total mass density profile of lens galaxies, i.e., what is the distribution function of γ' (see § 6.2). This is relevant not only in terms of formation scenarios but also in many applications of lensing. For example, cosmological parameters from lens statistics are generally obtained assuming that lenses are isothermal (e.g., Turner et al. 1984; Fukugita et al. 1990; Kochanek 1996; Helbig et al. 1999; Falco et al. 1998; Chae et al. 2002; Mitchell et al. 2004). Similarly, the Hubble constant from gravitational time delays (Refsdal 1964) is typically obtained assuming isothermal mass density profiles as well (e.g., Kundić et al. 1997a; Schechter et al. 1997; Impey et al. 1998; Biggs et al. 1999; Koopmans & Fassnacht 1999; Koopmans 2001; Kochanek 2002b; Wucknitz et al. 2004). In addition, estimating the central stellar velocity dispersion σ from lens models depends on the assumed mass model. Hence, how justified is the isothermal approximation?

The main conclusion from § 6.2 is that there appears to be intrinsic scatter in the values of γ' for lower values of R_{Einst}/R_e. A possible trend is seen, with γ' increasing with R_{Einst}/R_e and reaching $\gamma' \approx 2$ at large relative radii. However, based only on five systems, it is dangerous to interpret this as a real physical trend. For example, the two other lenses for which we have done a similar analysis, PG 1115+080 (TK02b) and B1608+656 (K03), not selected as part of the LSD Survey,[16] have $\gamma' > 2$ ($\gamma' = 2.35 \pm 0.1 \pm 0.1$ and $2.03 \pm 0.1 \pm 0.1$, respectively). By including those in the plot (Fig. 8, open triangles), the scatter in γ' would increase at low values of R_{Einst}/R_e, erasing any apparent trend. The straight average for this extended sample becomes $\langle \gamma' \rangle = 1.9 \pm 0.1$ with an rms of 0.3 for the isotropic case ($r_i = \infty$). Hence, with a larger sample in hand, one might indeed find that γ' approaches ≈ 2 but also that there is significant intrinsic scatter (see also R03b, who statistically build a mass profile from a sample of lens galaxies and find $\langle \gamma' \rangle = 2.07 \pm 0.13$). Is such a large scatter expected? At the radii of interest, typically of the order of the effective radius, we can expect scatter for at least two reasons.

First, E/S0 galaxies are typically found in or near groups or clusters, and we expect that E/S0 lens galaxies will be in a similar environment (see discussion on the C0302 lens model). A group dark matter halo might be present around the lens (a cluster will be external, since they are critical themselves and would produce much larger image separations). If the inner mass slope of the group halo is shallower than isothermal (as typically found in the inner regions of groups/clusters; e.g., Ettori et al. 2002; Kelson et al. 2002; Gavazzi et al. 2003; Kneib et al. 2003; Sand et al. 2002, 2004), it could introduce a "floor" of dark matter that will result in $\gamma' < 2$ (corresponding to the rising velocity dispersion profiles observed in some elliptical galaxies at the center of clusters; e.g., Dressler 1980;

---

[14] An additional source of uncertainty is due to the mass profile of the luminous component: the contours of γ' shift toward slightly lower values by adopting a Jaffe model for the luminous component.

[15] We note that the lens galaxies are not a statistical sample by any means, so the results should be interpreted as an exploration of the variety of possible behaviors rather than in a rigorous statistical sense.

[16] This is because they fail to meet the criteria of favorable contrast between the lens and the source.
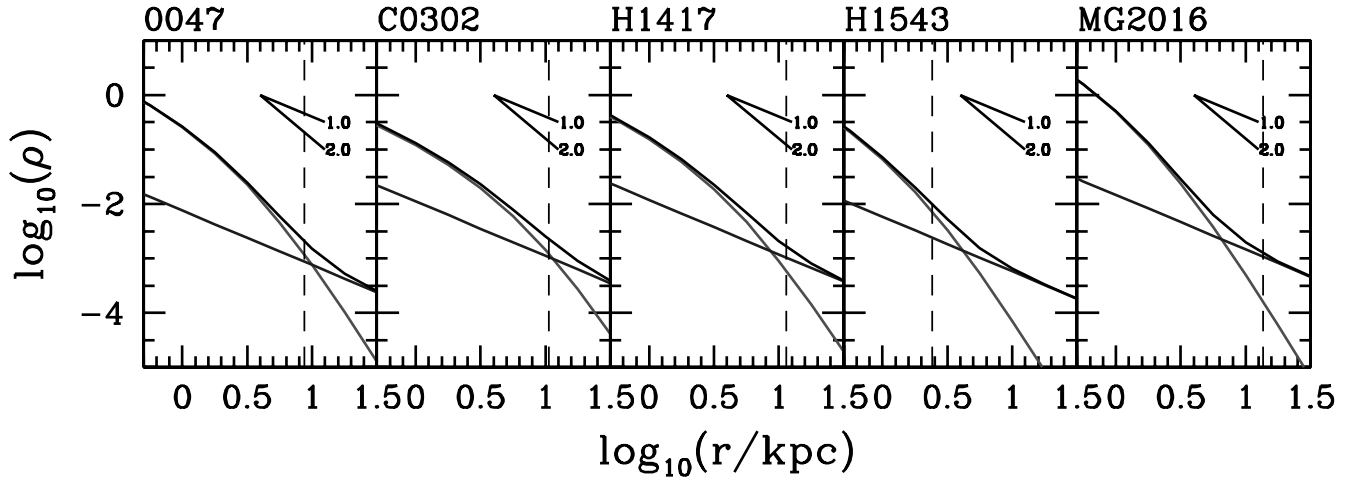
FIG. 11.—Density profiles of the five high-z LSD lens systems, representing the most likely isotropic ($r_i = \infty$) model for a dark matter halo with $\gamma = 1$ ($\rho_{\rm DM} \propto r^{-\gamma}$) and a Hernquist stellar mass density profile. The total mass density profile is plotted as a solid black line. The two bottom lines represent the stellar (dominant in the inner regions) and dark matter density profiles. The density is in units of $10^{10} \, M_\odot$ kpc^{-3}, and the dashed line indicates the Einstein radius. The two slopes for $\gamma' = 1$ and 2 are indicated for reference. [*See the electronic edition of the Journal for a color version of this figure.*]

Carter et al. 1985). Arguments suggesting that H1543, C0302, and possibly H1417 might be located in or near groups were presented in the previous sections. We emphasize that this is different from an intervening mass sheet, since the group is physically centered on or close to the lens galaxy and thus also affects the stellar dynamics. On the other hand, if the Einstein radius is small enough, the total mass distribution will become more dominated by the luminous component, which is typically steeper than isothermal and results in $\gamma' > 2$. At face value, the trend seen in Figure 8 is opposite to what we would expect: for small $R_{\rm Einst}/R_e$, where baryons dominate, we would expect $\gamma' > 2$, while at larger radii, where the group halo dominates, we would expect $\gamma' < 2$. Given the present size of the sample of five systems, the argument is inconclusive. The possible trend could simply result from C0302 and H1543 being in or near groups and thus having a larger dark matter floor than the other three lenses. However, this would be the opposite trend to, e.g., PG 1115+080, which shows a steeper than isothermal mass profile (TK02a) and is also close to a group (Kundić et al. 1997a). A possible mechanism to explain steepening of the mass density profile of the lens through interaction with a group/cluster could be tidal stripping (e.g., Natarajan et al. 2002; TK03) of the outer halo. Thus, if the lens was located at the center of the group/cluster, where a significant amount of cluster dark matter is present, the observed profile could be flatter than isothermal because of the dark matter floor. Vice versa, if the lens had been through the cluster/group center, deep enough to experience tidal stripping, but was observed on an outbound orbit far enough from the pericenter, the dark matter floor would no longer be relevant and a steeper profile would be observed.

Second, could the internal structure of luminous and dark matter in these E/S0 galaxies alone explain a trend or large scatter? In the local universe, we know that "rotation" curves of early-type galaxies show quite a variety of slopes within 1–2 effective radii (e.g., Bertin et al. 1994; Gerhard et al. 2001; Romanowsky et al. 2003), from rising ($\gamma' < 2$) to declining ($\gamma' > 2$). We might expect that the average and scatter of γ' would depend on the ratio between the Einstein radius and the effective radius and the fraction of dark matter $f_{\rm DM}$ contributing to the mass inside the Einstein radius. The larger

this ratio, the smaller the effect of baryons, and the more γ' will be a probe of the dark matter effective slope (possibly including some effects of nearby clusters or groups). In this case γ' will increase in three stages (see Fig. 11): First, for $r < r_*$ (see § 5), the slope is typically dominated by luminous mass and will have $\gamma' < 2$ for an $R^{1/4}$ profile. Second, for $r > r_*$, a transition takes place where dark matter becomes more prominent and the combination of luminous plus dark matter adds to an effective slope of $\gamma' \approx 2$. However, in the case that the fraction of dark matter ($f_{\rm DM}$) inside $R_{\rm Einst}$ is relatively small, one can expect that a very rapid transition can occur to $\gamma' > 2$ (e.g., PG 1115+080), if the luminous component remains dominant at $r \gtrsim r_*$ for $R_{\rm Einst}$ somewhat larger than r_*. Clearly this is very sensitive to $f_{\rm DM}$ and $R_{\rm Einst}/R_e$ and small variations in their value can induce large fluctuations in γ' for lenses with $R_{\rm Einst}/R_e \lesssim 1$. For larger values of $R_{\rm Einst}/R_e$, the larger radial range covered will result in less scatter for the same changes in $f_{\rm DM}$. Third, around the break radius, a transition is expected from the region where $\gamma' \approx 2$ to a dark matter–dominated regime where $\gamma' \approx 3$ (see, e.g., Seljak 2002 and Kneib et al. 2003 for a discussion of mass distribution at large radii from weak-lensing studies).

It seems to us that most likely a combination of the effects discussed above is required to interpret the observed trends and scatter in γ'. Group and cluster halos exist and must necessarily play a role (e.g., Lehar et al. 1997; Kundić et al. 1997a, 1997b; Tonry 1998; Tonry & Kochanek 1999, 2000; Blandford et al. 2001; Keeton et al. 2000; Fassnacht & Lubin 2002; Johnston et al. 2003). However, a model where galaxies are simply isothermal and appear more shallow if embedded in a group/cluster halo is not sufficient to explain the observations. Some degree of internal scatter in the properties of the dark matter halos of early-type galaxies is required. This scatter could be the result of complex and hierarchical formation history and baryonic cooling history and/or could be related to environmental effects (TK02b; Treu et al. 2003; Natarajan et al. 2002).

Ultimately, whatever the underlying cause or interpretation, we cannot escape the conclusion that the inner total mass profile of E/S0 galaxies at $z \approx 0.5-1.0$ is *on average* close to or slightly more shallow than isothermal *but also* that there

is a significant intrinsic rms scatter in γ' of up to $\sim$0.3 (i.e., $\sim$15% in density slope or $\sim$30% in surface density slope).

7.2. *Lensing Implications of Inhomogeneity*

In the previous subsection we concluded that E/S0 lens galaxies are close to isothermal on average, but not quite, and that there is a significant intrinsic scatter in the power-law slope of their total inner mass profiles. Here we briefly discuss the consequences of our finding on three important applications of gravitational lensing: (1) the determination of the Hubble constant from gravitational time delays, (2) the determination of the star formation history of E/S0 galaxies from image-separation estimates of the FP, and (3) the determination of the cosmological parameters from lens statistics.

Let us first consider the determination of the Hubble constant from gravitational time delays and consider a lens with unknown mass profile, modeled as SIEs. The observed rms scatter in γ' of $\sim$0.3 translates into a systematic uncertainty on H_0 of $\sim$30%, in addition to other uncertainties. For example, an rms of $\sim$20 km s^{-1} Mpc^{-1} can be expected if the true value is, say, $H_0 = 65$ km s^{-1} Mpc^{-1}. This range of 45–85 km s^{-1} Mpc^{-1} covers the vast majority of determinations of H_0 that assume isothermal mass profiles (e.g., Schechter et al. 1997; Impey et al. 1998; Biggs et al. 1999; Koopmans & Fassnacht 1999; Kochanek 2002a, 2002b; K03; Wucknitz et al. 2004) and could therefore in principle explain the mutual inconsistency between the inferred values of H_0. Different samples based on only a few lens systems could therefore lead to completely different conclusions (e.g., Koopmans & Fassnacht 1999; Kochanek 2002a, 2002b), if γ' is not determined for each system directly.

In TK02b and K03, we applied the lensing and dynamics analysis described above to two lens systems with measured time delays, finding power-law slopes of $\gamma' = 2.35 \pm 0.1 \pm 0.1$ and $2.03 \pm 0.1 \pm 0.1$ for PG 1115+080 and B1608+656, respectively, which lead to values of H_0 of $59^{+12}_{-7} \pm 3$ and $75^{+7}_{-6} \pm 4$ km s^{-1} Mpc^{-1}. In the case of PG 1115+080, a 35% increase was found for the value of H_0 from that expected from an isothermal model with $\gamma' = 2$ (i.e., $H_0 = 44$ km s^{-1} Mpc^{-1}; Impey et al. 1998). A difference in slope of 0.3 between these systems is fully consistent with the rms scatter in γ' that we find in our sample and thus "in hindsight" may not totally be unexpected.

Indeed, in this paper we have presented three lens galaxies with deviations of γ' in the opposite direction. Those systems would lead to severe overestimates of H_0 if they were assumed to be isothermal. As we have stressed before, one can overcome these problems by directly measuring the mass profile with a combination of lensing and stellar dynamics, or other methods (e.g., Wucknitz 2004). The statistical approach (i.e., lens galaxies are "on average" isothermal) is not (yet) satisfactory, since the average value of γ' and its scatter are poorly determined at present. For example, if the current samples of about four to five lenses (e.g., Koopmans & Fassnacht 1999; Kochanek 2002a, 2002b) were drawn from a Gaussian distribution of slopes with $\langle\gamma'\rangle \equiv 2$ and a 1 σ width of 0.3, one would most likely find many "outliers" (based on errors that do not incorporate the uncertainty in the mass profile) with very low or high inferred values of H_0. The distribution of γ' for a sample of lenses might also depend on unknown selection functions, and it appears therefore preferable to obtain a direct measurement of the mass slope (γ') for lenses with time delays.

Let us now turn our attention to the star formation history of early-type galaxies. Can we use multiple-image separation to estimate the central stellar velocity dispersion of E/S0 galaxies to construct an FP of lens galaxies and measure the evolution of their mass-to-light ratio (Kochanek et al. 2000; R03b; vdV03)? What is the accuracy of this approximation? Based on our sample, we find that $\langle f_{\mathrm{SIE}}\rangle < 1$. Hence, if we had used the isothermal model to determine the central velocity dispersion of our lenses from image separation, we would have overestimated their effective mass ($\sigma^2 R_e$) and underestimated the evolution of M_*/L_B. If $\langle f_{\mathrm{SIE}}\rangle$ was redshift independent, it would cancel out by fitting simultaneously the local intercept (as done by R03b), impacting the measurement only through the increased uncertainty due to the intrinsic scatter in $\langle f_{\mathrm{SIE}}\rangle$. However, this could be a redshift-dependent effect, since, for example, the ratio of the Einstein radius to the effective radius could depend on the redshift of the lens, and therefore it could mimic evolutionary trends. Hence, if the results from our sample of five E/S0 lens galaxies hold for the larger sample of lens systems, it could explain why most direct measurements (e.g., T02; Gebhardt et al. 2003; van der Wel et al. 2004; this paper) indicate a slightly faster evolution of the FP of E/S0 galaxies with redshift than those based on lens estimates of σ (e.g., R03b; vdV03). If this difference (at the moment only marginally significant) was confirmed by more precise measurements, it would be interesting to reverse the argument. If the lens-based estimate of the evolution of the FP is slower than the direct measurement, then the power-law slope of lens galaxies is on average flatter than isothermal and $\langle f_{\mathrm{SIE}}\rangle < 1$. The difference in the evolutionary rates would provide another measurement of $\langle f_{\mathrm{SIE}}\rangle$ and more importantly on $\langle\gamma'\rangle$.

Finally, we briefly discuss the effects on lensing statistics. If galaxies have $\langle f_{\mathrm{SIE}}\rangle < 1$ and $\gamma' = 2$, then statistical models that use isothermal lens mass models with $\sigma_{\mathrm{SIE}} = \sigma$ will tend to underestimate the lensing cross section of a population of lenses, since the correct $\sigma_{\mathrm{SIE}} = \sigma/f_{\mathrm{SIE}} > \sigma$. However, since we have found that $f_{\mathrm{SIE}} < 1$ for many lenses might actually be associated with $\gamma' < 2$, the effect is not so clear, since galaxies with more shallow mass profiles have lower lens cross sections for a fixed enclosed mass. On the other hand, they are more massive when normalized to the same σ (i.e., a shallower profile lowers σ for a fixed mass; hence, to increase it to the same value as for a steeper profile, its mass needs to be increased). We are generally in the latter situation, since statistical models are typically normalized to an observed distribution function of σ. It becomes even more complex, however, since all these effects need to be integrated over a distribution function of γ' and effects of the magnification bias as a function of mass profile need to be accounted for. The full treatment of this problem goes beyond the scope of this paper and is left for future research.

To summarize, the main conclusion of this section is that a simple isothermal model is probably not appropriate for precision measurements, especially when only small samples are available, as it is typically the case. The observed scatter does not seem surprising, given, for example, the wide range of velocity dispersion profiles observed for early-type galaxies, from declining to increasing with radius (see, e.g., Gerhard et al. 2001; Kelson et al. 2002). Unfortunately, the samples are still too small and the selection functions too poorly characterized to find out what is the *distribution* of total mass density profiles and whether the distribution for lens samples differs from the one from morphologically selected or X-ray–selected samples. As far as the lenses are concerned, at this stage the average slope appears to be slightly shallower than isothermal, in marginal contrast with other determinations, using different

methods and samples (e.g., R03b). Although the difference is relevant for precision measurements (e.g., of H_0) based on statistical arguments, we believe that what is remarkable is the relative agreement on the peak of the distribution being around $\gamma' = 2$, given the small size of the samples and the unknown sample selection biases. A larger number of lenses with precisely measured mass density profiles is needed to make further progress on these issues.

8. SUMMARY

We have presented new spectroscopic measurements for three gravitational lens systems, C0302 ($z = 0.938$), H1543 ($z = 0.497$), and H1417 ($z = 0.81$), as part of the Lenses Structure and Dynamics (LSD) Survey. Long integrations with ESI at the Keck II telescope have yielded extended stellar velocity dispersion profiles of all three lens E/S0 galaxies, extended approximately to the effective radius. A blue spectrum taken with LRIS-B has revealed the redshift of the lensed arc in H1543 ($z = 2.092$). Together with two previously published systems, MG 2016 ($z = 1.004$; TK02a; see also Koopmans et al. 2002) and 0047 ($z = 0.485$; KT03), this paper presents the analysis of the current high-redshift sample ($z \approx 0.5$–1.0), consisting of five pressure-supported E/S0 galaxies.

The spectroscopic data have been combined with surface photometry from *HST* archival images to study the evolution of the stellar populations via the evolution of the intercept of the fundamental plane (FP). For the sample of five LSD lenses we find $d \log (M/L_B)/dz = -0.72 \pm 0.10$, i.e., 1.80 ± 0.25 mag of dimming between $z = 1$ and 0. In a pure luminosity evolution scenario, this measurement can be interpreted as the result of a relatively young luminosity-weighted age of the stellar populations. A scenario in which most of the stars were formed at high redshift (>2) while a small fraction of stars ($\sim 10\%$) are formed in secondary bursts between $z = 1$ and 0 provides a simple explanation for this result, as well as several independent pieces of evidence (evolution of the luminosity function of E/S0 galaxies, spectroscopic evidence of recent minor episodes of star formation in distant E/S0, properties of local E/S0; see the discussion in § 3).

New gravitational lens models of the three systems C0302, H1417, and H1543 have been presented. H1417 has the classical "quad" morphology and can be successfully modeled with a singular isothermal ellipsoid (SIE) mass distribution, with an external shear and a gradient in the local convergence that roughly aligns with the galaxy major axis and that we interpret as an internal asymmetry in the galaxy. In contrast, the lens systems C0302 and H1543 are characterized by a source lensed into extended arclike features. These systems are modeled with an algorithm that allows for a non-parametric image reconstruction (see Appendices A, B, and C), incorporating some of the techniques by W96 and WD03. Both lenses are successfully modeled with an SIE mass model with external shear. In the case of H1543, a nearby (4″7) massive galaxy at the same redshift as the main lens is included in the lens model as a singular isothermal sphere (SIS). The Einstein radii ($R_{\rm Einst}$), SIE velocity dispersions ($\sigma_{\rm SIE}$), and enclosed masses ($M_{\rm Einst}$) of the three lenses are used to perform a joint lensing and dynamical analysis, with the following results:

1. Constant mass-to-light ratio models (i.e., mass follows light) are rejected at better than 99% CL for all five E/S0 lens galaxies. A dark matter halo with a mass density profile flatter than the luminous component is needed in all cases. The fraction of dark matter inside the Einstein radius ($f_{\rm DM}$) is 37%–72% (isotropic stellar orbits) and 15%–65% inside the effective radius.

2. Modeling the total mass density profile of the lenses as a single power-law density distribution $\rho_{\rm tot} \propto r^{-\gamma'}$, the effective slope γ' is found to be on average somewhat smaller than isothermal, i.e., $\langle \gamma' \rangle = 1.75$ with an rms scatter of 0.20 (for isotropic velocity ellipsoid; $\langle \gamma' \rangle = 1.57$ with an rms of 0.35 for radial anisotropy) for our sample of five lenses. If we include the two other systems that have a similar analysis, these values increase by ~ 0.15 and the rms increases to ~ 0.30. Consistent with these findings, the ratio $f_{\rm SIE} = \sigma/\sigma_{\rm SIE}$ between central velocity dispersion and velocity dispersion of the SIE mass model that best fits the lensing constraints is $\langle f_{\rm SIE} \rangle = 0.87$ with an rms scatter of 0.08.

3. The average mass-to-light ratio of the luminous component $\langle M_*/L_B \rangle = 2.3 \pm 0.6$ h_{65} $M_\odot$ $L_{B,\odot}^{-1}$ is smaller than the average value for early-type galaxies in the local universe, 7.3 ± 2.1 h_{65} $M_\odot$ $L_{B,\odot}^{-1}$, consistent with passive evolution of a relatively old stellar population. The stellar mass-to-light ratio obtained from the joint lensing and dynamics analysis is found to evolve as $\langle d \log (M/L_B)/dz \rangle = -0.75 \pm 0.17$, in excellent agreement with the independent measurement obtained via the FP.

4. The most precise constraints to date are obtained on the inner slope of the dark matter halo γ. We find the following 68% confidence limits: $\gamma < 0.58$ (anisotropic velocity ellipsoid with $r_i = R_e$) and $0.93 < \gamma < 1.48$ or $\gamma = 1.3^{+0.2}_{-0.4}$ (68% CL) for $r_i = \infty$. Thus, our data are consistent with CDM numerical simulations (with $\gamma = 1$–1.5) only if the velocity ellipsoid is not significantly radially anisotropic and baryonic collapse, during galaxy formation, did not significantly steepen the mass density profile as would be expected in simple adiabatic contraction scenarios (Blumenthal et al. 1986; Mo et al. 1998; Keeton 2001; Kochanek 2002b).

9. CONCLUSIONS

In conclusion, the following picture seems to be emerging from the analysis of the complete high-redshift LSD sample. High-redshift early-type galaxies are approximately isothermal ellipsoids, but not exactly. Our current sample seems to indicate that on average the effective slope of the mass density profile inside the Einstein radius might be slightly smaller than 2, i.e., total mass density profile flatter than isothermal, albeit $\gamma' = 2$ is generally within the range of the distribution (e.g., the first two objects we analyzed were almost exactly isothermal; TK02a; KT03). A possible cause for departure from homogeneity could be the environment of early-type galaxies. Contributions from a relatively flat group or cluster dark matter halo could introduce a floor of mass at the position of the lens, causing the total mass density profile to appear effectively flatter. Independent external evidence (such as the presence of nearby galaxies at the same redshift) indicates that possibly all three lenses for which we found $\gamma' < 2$ might be members of a group, and therefore this mechanism would appear to be a likely explanation, at least for this sample. However, this mechanism does not appear to be sufficient to account for all the observed scatter because most of the scatter is observed for $R_{\rm Einst}/R_e < 1$, where the galaxy mass distribution should dominate over a group halo, and because there

are cases where $\gamma' > 2$ is observed (such as PG 1115+080 and B1608+656; the former also has a nearby compact group). We therefore conclude that the scatter in the total mass density profile is associated with intrinsic scatter in the ratio of dark matter to luminous matter in the inner regions of high-redshift early-type galaxies, similar to what is observed in the local universe (Bertin & Stiavelli 1993; Bertin et al. 1994; Gerhard et al. 2001).

Regardless of the physical interpretation, the observed scatter in the effective slope (i.e., 10%–15% in density slope) still implies a remarkable degree of structural homogeneity between early-type galaxies from a galaxy formation point of view. Whatever the details of the mass assembly and star formation history, E/S0 galaxies end up being close to isothermal, for example, expected in (incomplete) violent relaxation scenarios (Lynden-Bell 1967; Shu 1978; van Albada 1982; Bertin & Stiavelli 1993; Hjorth & Madsen 1991, 1995). From an evolutionary point of view, the intrinsic scatter in the mass density profiles of high-redshift E/S0 galaxies does not seem to be much different from that of local E/S0 galaxies, providing no evidence for much structural evolution within the last 4–8 Gyr.

Although the homogeneity is remarkable from a galaxy formation point of view, the observed scatter in γ' is large enough that the isothermal approximation might not be good for some applications, particularly when they depend critically on the mass slope. Meaningful examples include the determination of H_0 from gravitational time delays, where a scatter of ~ 0.3 in γ' translates into a scatter of $\sim 30\%$ in H_0 for a given time delay (Saha 2000; Wucknitz 2002; Kochanek 2002b; TK02b). Thus, it appears necessary to use external information, such as internal kinematics, to pinpoint γ' and H_0 to a level of accuracy (10%–15%) competitive with other methods (K03; see also Wucknitz et al. 2004). A precision measurement based on statistical assumptions of γ' will probably have to wait until the distribution of γ' is observationally well characterized and a large enough sample of lenses with time delays is available to minimize variance.

The other main result of this paper is the decomposition of the total mass distribution into a luminous component and a dark matter halo. High-redshift early-type galaxies are inconsistent with constant mass-to-light ratio mass models. The mass-to-light ratio has to increase significantly with radius, consistent with the presence of dark matter halos flatter than the luminous component (dark matter makes up a substantial fraction of the mass of the lenses inside the Einstein radius, of order 40%–70%).

The mass-to-light ratio of the luminous component is smaller than in the local universe, consistent with passive evolution of a relatively old stellar population. The agreement between the evolution of the stellar mass-to-light ratio measured directly and that determined from the evolution of the intercept of the FP is another argument against strong structural and dynamical evolution. If early-type galaxies had changed their mass distribution significantly between $z \sim 1$ and today, they would have to be doing so while preserving the mapping between velocity dispersion, radius, and stellar mass. A simpler (and to our eyes preferable) explanation would be one involving no or little dynamical evolution.

The precise mass density profile of the dark matter halos is harder to constrain, since most of the mass at small radii is luminous. Nevertheless, our sample of five lenses allows us for the first time to set limits on the inner dark matter density slope γ that are interesting to compare with cosmological simulations. Our measurement can be reconciled with numerical cosmological only if (1) the velocity ellipsoid is not significantly radially anisotropic and (2) the collapse of baryons to form the galaxy did not steepen the dark matter halo more than a few tenths in γ. The latter constraint is clearly inconsistent with simple adiabatic collapse models (Blumenthal et al. 1986) and suggests that different mechanisms are involved in the accretion of stars of the centers of the halos of early-type galaxies. This is further supported by lensing statistics results, which imply a low value of $f_{DM}(< R_e) < 0.33$ (95% CL; Keeton 2001). Assuming adiabatic contraction implies that the initial slope (γ_i) of the dark matter halo (i.e., before contraction) was shallower than predicted from ΛCDM models (i.e., $\gamma_i < 1$) and introduces an additional inconsistency. Mechanisms such as those proposed for clusters (El-Zant et al. 2004; Nipoti et al. 2003), where stars form first in satellites, which are then accreted as dissipationless particles, could provide the desired effect (see also Loeb & Peebles 2003), although a detailed comparison of data with theory will have to wait until cosmological simulations including a realistic treatment of star formation become available.

APPENDIX A

DELENSING OF IMAGES ON A GRID

Suppose we have a lensed image, $\hat{d}$, on a grid[17] (e.g., a CCD image) in which all emission not associated with the lensed source has been masked and/or subtracted. Hence, the grid should be a noisy, blurred, and lensed representation of the true underlying source brightness distribution, which it is our aim to reconstruct. Suppose also that we can construct a lens operator L (depending on the parameters of our lens model) that, acting on a source grid $\hat{s}$, produces a lensed image of the source. Suppose further that a blurring operator, B, exists that, acting on $L\hat{s}$, produces a blurred lensed image. Putting this together, we have

$$BL\hat{s} = \hat{d}_t + \hat{n}, \tag{A1}$$

where $\hat{n}$ represents the noise in the observed image and $\hat{d}_t = \hat{d} - \hat{n}$ is the noise-free lensed image. Note that the size or shape of the image and source grids and their pixel sizes are irrelevant to the problem. Furthermore, neither the grid nor the pixels have to be rectangular and connected (e.g., the image grid could have a gap). As long as the value of each observed pixel can be written as a linear combination of source-pixel values, the above equation is applicable. For simplicity, however, we assume rectangular grids and pixels for the remainder of this paper. Naively, one would think that the solution to this problem, i.e., the source brightness distribution, can easily be found by inverting the above equation through $\hat{s} = (BL)^{-1}\hat{d}$. However, this is a notoriously ill-posed problem, and noise in the observed image will typically lead to unacceptably poor reconstructions. We do not discuss this solution further. The problem can be regularized, however, suppressing the effects of $\hat{n}$ on the final source reconstruction. Mathematically, we would like to find the source grid $\hat{s}$ and the parameters of the lens model (i.e., L) that minimize the following equation:

$$C(\lambda) = \left\| BL\hat{s} - \hat{d} \right\|_2^2 + \lambda \| H\hat{s} \|_2^2, \tag{A2}$$

where H is a regularization operator and λ determines the weight given to the regularization term. For simplicity we have also written $(BL)/\hat{n} \rightarrow (BL)$ and $\hat{d}/\hat{n} \rightarrow \hat{d}$ (see Press et al. 1992). The first term in equation (A2) is simply the χ^2 term, whereas the second term regulates the "smoothness" of the final solution. In particular, if $H = I$, then the regularization term is simply the sum over the squared pixel values in the source grid. The latter term, however, can also regulate the smoothness of the derivatives in the source grid or be replaced by a maximum likelihood or maximum entropy term. The solution to equation (A2) is the solution to the set of linear equations

$$\left[(BL)^T(BL) + \lambda H^T H \right] \hat{s} = (BL)^T \hat{d}. \tag{A3}$$

This equation has a unique solution, thanks to the regularization term, and can be solved through standard techniques and using freely available linear algebra packages for large sparse matrices.

APPENDIX B

THE LENSING AND BLURRING OPERATORS

The main problem that is faced in constructing a lens operator is the fact that an image pixel, when projected on the source grid, in general will not exactly coincide with a source pixel. One way to solve this (WD03) is to determine the lensed image for a given source pixel of unit flux, blurred by the PSF and regridded to the image grid. This is repeated for all source pixels. The source is then reconstructed by finding the set of source-pixel weights (i.e., fluxes for each source pixel) and the corresponding lensed images, for which their linear combination best reconstructs the observed image. This requires inverting the lens equation and is numerically expensive for complex models. It also requires finding all lensed images for each pixel. There are no simple algorithms that guarantee this for complex mass models.

However, one can also construct a lens operator that does not require the lens inversion. Before describing this, we first introduce some definitions. We assume that the source grid has $K \times L$ pixels (K columns and L rows) and similarly the (as of yet unblurred) image grid, $\hat{d}'$, has $M \times N$ pixels. The values of each pixel are $s_{k,l}$ and $d'_{m,n}$, respectively. Hence, $\hat{s} = \{s_{i=k+(l-1)K}\}$ with $i = 1 \ldots KL$ with $k = 1 \ldots K$ and $l = 1 \ldots L$. Similarly, $\hat{d}' = L\hat{s} = \{d'_{j=m+(n-1)M}\}$ with $j = 1 \ldots MN$ with $m = 1 \ldots M$ and $n = 1 \ldots N$. It is now very easy to construct a particular implementation of the lens operator, L, which is a matrix of size $KL \times MN$ and entries $l_{i,j}$. We emphasize that our choice is not unique, but it is simple and fast. First, each pixel $j = m + (n-1)M$ is cast back on the source plane to a position y_j, using the lens equation. If the position is outside the (predefined) grid, one simply continues to the next pixel. In general, however, the lensed image grid and source grid will be defined to overlap as much as possible to reduce redundancy, although this is not a requirement. Second, one determines the four pixels in the source grid that enclose y_j, say, $(r + \mu, s + \nu)$ for $\mu = 0, 1$ and $\nu = 0, 1$. Suppose that the position of (r, s) is $y_{r,s}$ and $(t, u) = y_j - y_{r,s}$. The flux of pixel j can then be written as a linear combination of the four source-pixel fluxes

$$d'_j = \sum_{\mu=0}^{1} \sum_{\nu=0}^{1} w_{\mu,\nu} s_{i=(r+\mu)+(s+\nu-1)K}, \tag{B1}$$

---

[17] All two-dimensional grids are represented as vectors in which consecutive rows are placed behind each other.

where

$$w_{0,0} = (1 - t)(1 - u), \quad w_{1,0} = t(1 - u), \quad w_{0,1} = tu, \quad w_{1,1} = (1 - t)u. \quad (B2)$$

This is simply a bilinear interpolation of the four source-pixel fluxes, but more complicated linear schemes can be constructed, although they will generate more entries in the lens operator (except if one chooses to use an enclosing triangle). The four entries in the lens operator, at $l_{i,j}$, for image pixel j are then the values of $w_{\mu,\nu}$ at $i = (r + \mu) + (s + \nu - 1)K$ for $\mu = 0, 1$ and $\nu = 0, 1$. Finally, $\boldsymbol{L}$ contains at most $4MN$ entries.[18]

The next step is to construct the blurring operator, $\boldsymbol{B}$, that acts on the lensed image $\hat{\boldsymbol{d}}'$. As an illustration, suppose that the PSF is a square grid of size $(2H + 1) \times (2H + 1)$ pixels with values $p_{\mu,\nu}$ with $\mu = -H \ldots H$ and $\nu = -H \ldots H$ and peaks at $p_{0,0}$. The sum of the PSF pixels adds to unity. The entries in the blurring operator, $b_{g,h}$, are then simply the values of $p_{\mu,\nu}$ at $g = (h + \mu) + (h + \nu - 1)M$, if and only if $1 \leq (h + \mu) \leq M$ and $1 \leq (h + \nu) \leq N$ for each $h = 1 \ldots MN$.

Notice here that this method allows one to define a color-dependent blurring operator. In that case, for each h (i.e., pixel in the image plane), one can use a PSF with values $p_{\mu,\nu,h}$ that depend on the local color of the pixel. We also note that an extinction correction can be done by setting the integral over the PSF, $\Sigma_\mu \Sigma_\nu p_{\mu,\nu} = e^{-\tau} < 1$, where τ is the optical depth due to extinction. (Note that this requires a color and extinction model, since both effects occur *before* blurring.)

APPENDIX C

PRACTICALITIES IN THE OPTIMIZATION

The pixel size in the source plane is set roughly by the largest pixel magnification in the image plane. If the source-plane pixels are chosen too large, the resulting image shows the effects of the mapping of individual source-plane pixels. If they are chosen too small, however, the source breaks up in "strings" of pixels that map closely to the image-plane pixels, but no flux in between (e.g., for $\boldsymbol{H} = \boldsymbol{I}$). Mathematically these solutions are equivalent, but physically clearly not. We therefore set the pixel size such that the source does not tend to break up and adjacent image-plane pixels roughly map onto adjacent source-plane pixels. We then set λ to an initially large value of typically ~ 0.1 and minimize $C(\lambda)$ by varying the lens-model parameters (see WD03 for details). We then lower the value of λ slowly, continuing to optimize the model parameters, until a reduced χ^2 of unity is reached. In general, we find that the resulting mass model parameters are relatively robust against changes in either the source-plane pixel size or the value of λ, as long as the source remains compact, and we refer to WD03 for a more thorough discussion of different choices.

---

[18] Note that $\boldsymbol{L}$ contains a fraction of $\leq 4/(KL)$ nonzero elements. For a 100×100 image grid, this is $\leq 0.04\%$. It is obvious that sparse-matrix packages are required, or otherwise $\boldsymbol{L}$ alone would require ~ 1 GB of computer memory to store.

REFERENCES

Abazajian, K., et al. 2003, AJ, 126, 2081
Arnaboldi, M., et al. 1996, ApJ, 472, 145
Bartelmann, M., & Meneghetti, M. 2004, A&A, 418, 413
Bender, R., Saglia, R. P., Ziegler, B., Belloni, P., Greggio, L., Hopp, U., & Bruzual, G. 1998, ApJ, 493, 529
Benson, A. J., Ellis, R. S., & Menanteau, F. 2002, MNRAS, 336, 564
Bernardi, M., et al. 2003, AJ, 125, 1866
Bertin, G., Ciotti, L., & del Principe, M. 2002, A&A, 386, 149
Bertin, G., & Stiavelli, M. 1993, Rep. Prog. Phys., 56, 493
Bertin, G., et al. 1994, A&A, 292, 381
Biggs, A. D., Browne, I. W. A., Helbig, P., Koopmans, L. V. E., Wilkinson, P. N., & Perley, R. A. 1999, MNRAS, 304, 349
Binney, J., & Tremaine, S. 1987, Galactic Dynamics (Princeton: Princeton Univ. Press)
Blandford, R., Surpi, G., & Kundić, T. 2001, in ASP Conf. Ser. 237, Gravitational Lensing: Recent Progress and Future Go, ed. T. G. Brainerd & C. S. Kochanek (San Francisco: ASP), 65
Blumenthal, G. R., Faber, S. M., Flores, R., & Primack, J. R. 1986, ApJ, 301, 27
Blumenthal, G. R., Faber, S. M., Primack, J. R., & Rees, M. J. 1984, Nature, 311, 517
Borriello, A., Salucci, P., & Danese, L. 2003, MNRAS, 341, 1109
Brinchmann, J., et al. 1998, ApJ, 499, 112
Bullock, J. S., Kolatt, T. S., Sigad, Y., Somerville, R. S., Kravtsov, A. V., Klypin, A. A., Primack, J. R., & Dekel, A. 2001, MNRAS, 321, 559
Carollo, C. M., de Zeeuw, P. T., van der Marel, R. P., Danziger, I. J., & Qian, E. E. 1995, ApJ, 441, L25
Carter, D., Inglis, I., Ellis, R. S., Efstathiou, G., & Godwin, J. G. 1985, MNRAS, 212, 471
Chae, K.-H., et al. 2002, Phys. Rev. Lett., 89, 1301
Chen, H.-W., et al. 2003, ApJ, 586, 745
Cohn, J. D., Kochanek, C. S., McLeod, B. A., & Keeton, C. R. 2001, ApJ, 554, 1216
Crampton, D., Le Fevre, O., Hammer, F., & Lilly, S. J. 1996, A&A, 307, L53
Crampton, D., Schade, D., Hammer, F., Matzkin, A., Lilly, S. J., & Le Fèvre, O. 2002, ApJ, 570, 86

Dalal, N., & Keeton, C. K. 2003, preprint (astro-ph/0312072)
Davis, M., Efstathiou, G., Frenk, C. S., & White, S. D. M. 1985, ApJ, 292, 371
de Blok, W. J. G., & McGaugh, S. S. 1997, MNRAS, 290, 533
Diaferio, A., Kauffmann, G., Balogh, M. L., White, S. D. M., Schade, D., & Ellingson, E. 2001, MNRAS, 323, 999
Djorgovski, S. G., & Davis, M. 1987, ApJ, 313, 59
Dressler, A. 1980, ApJ, 236, 351
Dressler, A., Lynden-Bell, D., Burstein, D., Davies, R. L., Faber, S. M., Terlevich, R., & Wegner, G. 1987, ApJ, 313, 42
El-Zant, A., Hoffman, Y., Primack, J., Combes, F., & Shlosman, I. 2004, ApJ, 607, L75
Ettori, S., Fabian, A. C., Allen, S. W., & Johnstone, R. M. 2002, MNRAS, 331, 635
Fabbiano, G. 1989, ARA&A, 27, 87
Faber, S. M., & Gallagher, J. S. 1979, ARA&A, 17, 135
Falco, E. E., Kochanek, C. S., & Munoz, J. A. 1998, ApJ, 494, 47
Fassnacht, C. D., & Lubin, L. M. 2002, AJ, 123, 627
Franx, M. 1993, PASP, 105, 1058
Franx, M., van Gorkom, J. H., & de Zeeuw, P. T. 1994, ApJ, 436, 642
Fruchter, A. S., & Hook, R. N. 2002, PASP, 114, 144
Fukugita, M., Futamase, T., & Kasai, M. 1990, MNRAS, 246, 24P
Fukugita, M., Osamu, N., Turner, E. L., Helmboldt, J., & Nichol, R. C. 2004, ApJ, 601, L127
Gavazzi, R., Fort, B., Mellier, Y., Pelló, R., & Dantel-Fort, M. 2003, A&A, 403, 11
Gebhardt, K., et al. 2003, ApJ, 597, 239
Gerhard, O., Kronawitter, A., Saglia, R. P., & Bender, R. 2001, AJ, 121, 1936
Ghigna, S., Moore, B., Governato, F., Lake, G., Quinn, T., & Stadel, J. 2000, ApJ, 544, 616
Glazebrook, K., et al. 2004, ApJ, submitted (astro-ph/0401037)
Groth, E. J., et al. 1994, BAAS, 26, 1403
Hammer, F., Crampton, D., Le Fèvre, O., & Lilly, S. J. 1995, ApJ, 455, 88
Helbig, P., Marlow, D., Quast, R., Wilkinson, P. N., Browne, I. W. A., & Koopmans, L. V. E. 1999, A&AS, 136, 297
Hernquist, L. 1990, ApJ, 356, 359

Hjorth, J., & Madsen, J. 1991, MNRAS, 253, 703
———. 1995, ApJ, 445, 55
Im, M., Faber, S. M., Koo, D. C., Phillips, A. C., Schiavon, R. P., Simard, L., & Willmer, C. N. A. 2002, ApJ, 571, 136
Impey, C. D., Falco, E. E., Kochanek, C. S., Lehar, J., McLeod, B. A., Rix, H.-W., Peng, C. Y., & Keeton, C. R. 1998, ApJ, 509, 551
Jaffe, W. 1983, MNRAS, 202, 995
Jimenez, R., Verde, L., & Oh, S. P. 2003, MNRAS, 339, 243
Johnston, D. E., et al. 2003, AJ, 126, 2281
Jørgensen, I., Franx, M., Hjorth, J., & van Dokkum, P. G. 1999, MNRAS, 308, 833
Kauffmann, G. 1996, MNRAS, 281, 487
Keeton, C. R. 2001, ApJ, 561, 46
Keeton, C. R., Christlein, D., & Zabludoff, A. I. 2000, ApJ, 545, 129
Kelson, D. D., Illingworth, G. D., van Dokkum, P. G., & Franx, M. 2000, ApJ, 531, 137
Kelson, D. D., van Dokkum, P. G., Franx, M., Illingworth, G. D., & Fabricant, D. 1997, ApJ, 478, L13
Kelson, D. D., Zabludoff, A. I., Williams, K. A., Trager, S. C., Mulchaey, J. S., & Bolte, M. 2002, ApJ, 576, 720
Kneib, J.-P., Mellier, Y., Fort, B., & Mathez, G. 1993, A&A, 273, 367
Kneib, J.-P., et al. 2003, ApJ, 598, 804
Knudson, A., Ratnatunga, K. U., & Griffiths, R. E. 2001, AJ, 122, 103
Kochanek, C. S. 1991, ApJ, 371, 289
———. 1994, ApJ, 436, 56
———. 1995, ApJ, 445, 559
———. 1996, ApJ, 466, 638
———. 2002a, ApJ, 578, 25
———. 2002b, preprint (astro-ph/0204043)
Kochanek, C. S., et al. 2000, ApJ, 543, 131
Koo, D., et al. 1996, ApJ, 469, 535
Koopmans, L. V. E. 2001, Publ. Astron. Soc. Australia, 18, 179
Koopmans, L. V. E., & Fassnacht, C. D. 1999, ApJ, 527, 513
Koopmans, L. V. E., Garrett, M. A., Blandford, R. D., Lawrence, C. R., Patnaik, A. R., & Porcas, R. W. 2002, MNRAS, 334, 39
Koopmans, L. V. E., & Treu, T. 2002, ApJ, 568, L5 (KT02)
———. 2003, ApJ, 583, 606 (KT03)
Koopmans, L. V. E., Treu, T., Fassnacht, C. D., Blandford, R. D., & Surpi, G. 2003, ApJ, 599, 70 (K03)
Kormann, R., Schneider, P., & Bartelmann, M. 1994, A&A, 284, 285
Kundič, T., Cohen, J. G., Blandford, R. D., & Lubin, L. M. 1997a, AJ, 114, 507
Kundič, T., Hogg, D. W., Blandford, R. D., Cohen, J. G., Lubin, L. M., & Larkin, J. E. 1997b, AJ, 114, 2276
Lehar, J., et al. 1997, AJ, 114, 48
Lilly, S. J., Le Fèvre, O., Crampton, D., Hammer, F., & Tresse, L. 1995, ApJ, 455, 50
Loeb, A., & Peebles, P. J. E. 2003, ApJ, 589, 29
Loewenstein, M., & White, R. E. 1999, ApJ, 518, 50
Lombardi, M., Rosati, P., Nonino, M., Girardi, M., Borgani, S., & Squires, G. 2000, A&A, 363, 401
Lynden-Bell, D. 1967, MNRAS, 136, 101
Ma, C.-P. 2003, ApJ, 584, L1
Matsushita, K., Makishima, K., Ikebe, Y., Rokutanda, E., Yamasaki, N., & Ohashi, T. 1998, ApJ, 499, L13
Menanteau, F., Abraham, R. G., & Ellis, R. S. 2001, MNRAS, 322, 1
Merritt, D. 1985a, AJ, 90, 1027
———. 1985b, MNRAS, 214, 25P
Merritt, D., & Aguilar, L. A. 1985, MNRAS, 217, 787
Mitchell, J. L., Keeton, C. R., Frieman, J. A., & Sheth, R. K. 2004, ApJ, submitted (astro-ph/0401138)
Mo, H. J., Mao, S., & White, S. D. M. 1998, MNRAS, 295, 319
Moore, B., Governato, F., Quinn, T., Stadel, J., & Lake, G. 1998, ApJ, 499, L5
Mould, J. R., Oke, J. B., de Zeeuw, P. T., & Nemec, J. M. 1990, AJ, 99, 1823
Muñoz, J. A., Kochanek, C. S., & Keeton, C. R. 2001, ApJ, 558, 657
Natarajan, P., Kneib, J.-P., & Smail, I. 2002, ApJ, 580, L11
Navarro, J., Frenk, C. S., & White, S. D. M. 1996, ApJ, 462, 563
———. 1997, ApJ, 490, 493
Nipoti, C., Stiavelli, M., Ciotti, L., Treu, T., & Rosati, P. 2003, preprint (astro-ph/0311424)
Nipoti, C., Treu, T., Ciotti, L., & Stiavelli, M. 2004, MNRAS, submitted (astro-ph/0404127)
Ohyama, Y., et al. 2002, AJ, 123, 2903
Oke, J. B., et al. 1995, PASP, 107, 375
Osipkov, L. P. 1979, Pis'ma Astron. Zh., 5, 77
Pahre, M. 1998, Ph.D. thesis, Caltech
Press, W. H., Teukolsky, S. A., Vetterling, W. T., & Flannery, B. P. 1992, Numerical Recipes in FORTRAN (Cambridge: Cambridge Univ. Press)
Ratnatunga, K., Griffiths, R. E., & Ostrander, E. J. 1999a, AJ, 117, 2010
———. 1999b, AJ, 118, 86

Ratnatunga, K., Ostrander, E. J., Griffiths, R. E., & Im, M. 1995, ApJ, 453, L5
Refsdal, S. 1964, MNRAS, 128, 307
Rix, H. W., de Zeeuw, P. T., Cretton, N., van der Marel, R. P., & Carollo, C. M. 1997, ApJ, 488, 702
Romanowsky, A. J., et al. 2003, Science, 301, 1696
Rubin, V. C., Thonnard, N., & Ford, W. K. 1978, ApJ, 225, L107
———. 1980, ApJ, 238, 471
Rusin, D., Kochanek, C. S., & Keeton, C. R. 2003a, ApJ, 595, 29
Rusin, D., & Ma, C.-P. 2001, ApJ, 549, L33
Rusin, D., Norbury, M., Biggs, A. D., Marlow, D. R., Jackson, N. J., Browne, I. W. A., Wilkinson, P. N., & Myers, S. T. 2002, MNRAS, 330, 205
Rusin, D., et al. 2003b, ApJ, 587, 143 (R03b)
Saglia, R. P., Bertin, G., & Stiavelli, M. 1992, ApJ, 384, 433
Saha, P. 2000, AJ, 120, 1654
Salucci, P., & Burkert, A. 2000, ApJ, 537, L9
Sand, D. J., Treu, T., & Ellis, R. S. 2002, ApJ, 574, L129
Sand, D. J., Treu, T., Smith, G. P., & Ellis, R. S. 2004, ApJ, 604, 88
Schechter, P., et al. 1997, ApJ, 475, L85
Schlegel, D. J., Finkbeiner, D. P., & Davis, M. 1998, ApJ, 500, 525
Seljak, U. 2002, MNRAS, 334, 797
Sheinis, A. I., Bolte, M., Epps, H. W., Kibrick, R. I., Miller, J. S., Radovan, M. V., Bigelow, B. C., & Sutin, B. M. 2002, PASP, 114, 851
Shu, F. H. 1978, ApJ, 225, 83
Steidel, C. C., Giavalisco, M., Pettini, M., Dickinson, M., & Adelberger, K. 1996, ApJ, 462, L17
Stiavelli, M., & Sparke, L. 1991, ApJ, 382, 466
Swaters, R. A., Madore, B. F., & Trewhella, M. 2000, ApJ, 531, L107
Tonry, J. L. 1998, AJ, 115, 1
Tonry, J. L., & Kochanek, C. S. 1999, AJ, 117, 2034
———. 2000, AJ, 119, 1078
Trager, S. C., Faber, S. M., Worthey, G., & Gonzalez, J. J. 2000, AJ, 119, 1645
Treu, T. 2004, in Clusters of Galaxies: Probes of Cosmological Structure and Galaxy Evolution, ed. J. S. Mulchaey, A. Dressler, & A. Oemler (Cambridge: Cambridge Univ. Press), 178
Treu, T., Ellis, R. S., Kneib, J.-P., Dressler, A., Smail, I., Czoske, O., Oemler, A., & Natarajan, P. 2003, ApJ, 591, 53
Treu, T., & Koopmans, L. V. E. 2002a, ApJ, 575, 87 (TK02a)
———. 2002b, MNRAS, 337, L6 (TK02b)
———. 2003, MNRAS, 343, L29 (TK03)
Treu, T., & Stiavelli, M. 1999, ApJ, 524, L27
Treu, T., Stiavelli, M., Bertin, G., Casertano, C., & Møller, P. 2001a, MNRAS, 326, 237 (T01a)
Treu, T., Stiavelli, M., Casertano, C., Møller, P., & Bertin, G. 1999, MNRAS, 308, 1037 (T99)
———. 2002, ApJ, 564, L13 (T02)
Treu, T., Stiavelli, M., Møller, P., Casertano, C., & Bertin, G. 2001b, MNRAS, 326, 221 (T01b)
Turner, E. L., Ostriker, J. P., & Gott, J. R., III 1984, ApJ, 284, 1
van Albada, T. S. 1982, MNRAS, 201, 939
van Albada, T. S., & Sancisi, R. 1986, Philos. Trans. R. Soc. London, A320, 447
van den Bosch, F. C., Robertson, B. E., Dalcanton, J. J., & de Block, W. J. G. 2000, AJ, 119, 1579
van der Marel, R. P. 1994, MNRAS, 270, 271
van der Wel, A., Franx, M., van Dokkum, P. G., & Rix, H.-W. 2004, ApJ, 601, L5
van de Ven, G., van Dokkum, P. G., & Franx, M. 2003, MNRAS, 344, 924 (vdV03)
van Dokkum, P. G., & Ellis, R. S. 2003, ApJ, 592, L53
van Dokkum, P. G., & Franx, M. 1996, MNRAS, 281, 985
van Dokkum, P. G., Franx, M., Kelson D. D., & Illingworth G. D. 1998, ApJ, 504, L17
———. 2001, ApJ, 553, L39
van Dokkum, P. G., & Stanford, S. A. 2003, ApJ, 585, 78
Wallington, S., Kochanek, C. S., & Narayan, R. 1996, ApJ, 465, 64 (W96)
Warren, S. J., & Dye, S. 2003, ApJ, 590, 673 (WD03)
White, S. D. M., & Rees, M. J. 1978, MNRAS, 183, 341
Willis, J. P., Hewett, P. C., Warren, S. J., & Lewis, G. F. 2002, MNRAS, 337, 953
Winn, J. N., Rusin, D., & Kochanek, C. S. 2003, ApJ, 587, 80
Wucknitz, O. 2002, MNRAS, 332, 951
———. 2004, MNRAS, 349, 1
Wucknitz, O., Biggs, A. D., & Browne, I. W. A. 2004, MNRAS, 349, 14
Ziegler, B. L., Bower, R. G., Smail, I. R., Davies, R. L., & Lee, D. 2001, MNRAS, 325, 1571
Zwicky, F. 1937, ApJ, 86, 217